Influence of Jet Pressure on Multi-nozzle Supersonic Retropropulsion Flowfields

Xiuqi Yang

A thesis
submitted in partial fulfillment of the
requirements for the degree of

MASTER OF SCIENCE IN AERONAUTICS & ASTRONAUTICS

University of Washington

2019

Reading Committee:

Owen J. H. Williams, Chair

Adam P. Bruckner

Program Authorized to Offer Degree:
College of Engineering,
William E. Boeing Department of Aeronautics and Astronautics

University of Washington

Abstract

Influence of Jet Pressure on Multi-nozzle Supersonic Retropropulsion Flowfields

Xiuqi Yang

Chair of the Supervisory Committee:
Research Assistant Professor Owen J. H. Williams
Aeronautics & Astronautics

Multi-nozzle supersonic retropropulsion (SRP) is an often-desired configuration for maximum effectiveness of vehicle deceleration. However, the flowfields are difficult to examine due to three-dimensionality and unsteadiness is not well classified. This thesis experimentally investigates the influence of jet stagnation pressure on SRP flowfields of an inline tri-nozzle, similar to that of a Falcon 9 reentry burn configuration. A high-speed schlieren photography method capable of producing sharp and detailed image data at 76,000 Hz was used for flow visualization. Tests were conducted with jets located at the center of a perfectly expanded Mach 2 flow from a Ludwieg tube into room conditions. Comparisons are made with a range of single-jet configurations. Initial investigations corroborated earlier observations existence of a coherent bow shock oscillation unsteadiness at the equal jet and freestream stagnation pressures. The tri-nozzle SRP flowfield was observed to have an increase in directional asymmetry with increasing jet pressure. Bow shock penetration and rippling type unsteadiness were observed, similar to yet less frequent than a single nozzle with forebody, and very different from the coherent bow shock motion observed by Tan (2018). Despite two different types of unsteadiness, the maximum normalized bow shock movement was observed to be similar among all nozzle types, which suggests that similar mechanisms may underpin both types of unsteadiness.

TABLE OF CONTENTS

Page

List of Figures iii

Nomenclature vi

Chapter 1: Introduction 1
1.1 Motivation 1
1.2 Problems and Goals 4

Chapter 2: Background & Theory 9
2.1 Aerodynamic Drag Loss 9
2.2 Basic SRP Flowfield Features for Single and Multi-nozzle Configurations . . 11
2.3 Jet Expansion 14
2.4 SRP Flowfield Steadiness Regimes 15

Chapter 3: Experimental Appartus & Methods 18
3.1 Ludwieg Tube 18
3.2 Tri-nozzle Design and Verification 23
3.3 Comparison Nozzles 26

Chapter 4: Design and Test of the Schlieren System Incorporating an Overdriven LED Light Soruce 27
4.1 Optical Elements 27
4.2 Overdriven LED Light Source Development 34
4.3 Image Analysis 39

Chapter 5: Results and Discussion 41
5.1 Examination of Flowfield with Scale of Simple Nozzle 43
5.2 Tri-Nozzle Configuration 47

Chapter 6: Conclusion 60

References 62

Appendix A: Pulsed LED Circuits and Associated Components 64

Appendix B: Bow shock standoff distance normalized by jet hydraulic diameter . . . 66

LIST OF FIGURES

Figure Number Page

1.1 Simulated Apollo command module Mars entry trajectory in comparison with previous successful robotic missions with their ballistic coefficients listed $[kg/m^2]$ [1] 2
1.2 Flowfield of a center nozzle configuration on a forebody with key features labeled [2] 5
1.3 Simulation of central nozzle SRP flowfield transitioning from stable to unstable then back to stable as thrust coefficient increases [3] 5
1.4 Bow shock oscillating magnitude for $P_{0j}/P_{0\infty} = 1$, no shock penetration appearing [4] 6
1.5 Highly under-expanded jets interaction in a SRP flowfield [5] 7

2.1 Variation of drag coefficient due to increase in thrust coefficient for a simple forebody with a single, central nozzle arrangement [2] 10
2.2 Axial force difference between central nozzle configuration and peripheral nozzle configuration due to difference in drag preservation [6] 11
2.3 Flowfield features of the center nozzle configuration (a), and peripheral nozzle configuration (b) [2] 12
2.4 Simplified Falcon 9 first stage geometric specification, and the triple nozzle inline with z-axis are the ignited engines. [7] 13
2.5 Simulation of Falcon 9 first stage reentry burn at 37 km altitude, Mach 5.09 [8] 14
2.6 Jet expansion pattern into a quiescent medium: over-expanded (left), mildly under-expanded (middle), highly under-expanded (right)[9] 15
2.7 Left picture: 60-degree aero shell apparatus tested by Jarvinen and Adams (1970) [10]. Right picture: 70-degree aero shell forebody tested by Berry et al. (2011) [11] 16

3.1 The Ludwieg tube used as a supersonic wind tunnel 19
3.2 Ludwieg tube t-x diagram for an upstream-throat diaphragm [12] 20
3.3 The Mach 2 waveless nozzle used in the Ludwieg tube 21
3.4 Pressure and temperature ratios vs. area ratio [12] 21

3.5 The schematic of the double diaphragm breech with two bursting modes available 23
3.6 Tri-nozzle design drawing 24
3.7 Under-expanded tri-nozzle jets, vertical view 25
3.8 Under-expanded tri-nozzle jets, horizontal view 25
3.9 Dimensions of single nozzles used in the experiment 26

4.1 A basic single-mirror Schlieren system diagram: the incident beam does not take the same path as reflected beam 28
4.2 The image doubling effect on a single-mirror, coincident schlieren system: as the object to mirror distance increases, the image doubling becomes more severe 28
4.3 Schematic of light rays refracted by density fields with constant density and its first, second, and third derivative constant 29
4.4 Diagram of the knife-edge plane [13] 30
4.5 Tan (2018) schlieren system setup: the concave mirror was placed as close as possible to test section to reduce the image doubling 31
4.6 The average frame intensity of all test cases for Tan (2018) across all frames 32
4.7 Version 4 schematic: incident beam and reflected beam were merged co-linear by a beam splitter 33
4.8 Version 4 set up: the entire length of the schlieren system visible on the left picture, optical components near the high-speed camera on the right picture 33
4.9 Lincoln (2016) [14] pulsed LED circuit design 34
4.10 LED response to 4 μs square wave, breadboard prototype 36
4.11 LED response to 1 μs square wave, breadboard prototype 36
4.12 The experimental setup of the PCB verification test with critical equipment labeled 37
4.13 MOSFET on CH2 38
4.14 R_{sense} voltage drop on CH2 38
4.15 1 μs trigger 38
4.16 1 μs trigger, magnified 38
4.17 The comparison between Tan (2018) 39

5.1 All nozzle configurations 42
5.2 The mean image of SRP flowfield for all simple nozzles at all test conditions 44
5.3 The RMS image of SRP flowfield for all simple nozzles at all test conditions 45

5.4 Common features seen on a SRP flowfield labeled on 3/8" OD simple nozzle, P_0 ratio = 0.5 46
5.5 The nozzles used in the tri-nozzle study 47
5.6 The (left) mean image and (right) image of SRP flowfield comparison at P_0 Ratio = 5 48
5.7 The (left) mean image and (right) image of SRP flowfield comparison at P_0 Ratio = 1 49
5.8 The (left) mean image and (right) image of SRP flowfield comparison at P_0 Ratio = 0.5 50
5.9 Discontinuous"double band" feature near jet-to-jet interaction region 52
5.10 Large RMS downstream the highly visible expansion fan in the tri-nozzle horizontal orientation at P_0 ratio = 5 52
5.11 Common features of the flowfields are highlighted. Left picture: 1/8" simple nozzle with 3/8" forebody. Middle picture: tri-nozzle vertical orientation. Right picture: tri-nozzle horizontal orientation. 53
5.12 Bow shock standoff distance normalized by jet hydraulic diameter 55
5.13 Snapshots of all unsteady cases showing the maximum shock displacement magnitude 57
5.14 Normalized bow shock oscillation magnitude at P_0 ratio = 1 58

A.1 Design iteration of the LED circuit by Willert et al. (2010b) (left) Wilson et al. (2014) (middle), and Lincoln (2016) (right) 64

B.1 Bow shock standoff distance normalized by jet hydraulic diameter 67

NOMENCLATURE

a: Speed of sound

C: Contrast of a schileren image

C_A: Total axial force coefficient

C_D: Drag coefficient

C_T: Thrust coefficient

D: Drag force

f: Focal length of a lens or a mirror

k: Gladstone-Dale coefficient

M: Mach number

m: Mass

n: Refractive index

p: Pressure

q: Dynamic pressure

S: Schlieren sensitivity

T: Temperature

β: Ballistic coefficient

γ: Specific heat ratio

ACKNOWLEDGMENTS

First and foremost, I would like to thank my advisor, Professor Owen Williams. I could not ask for a better mentor who guided me through difficult problems with patience and care in the past two years. I learned much in academics and gained high confidence in stepping into the future.

I would like to thank my mentor, Professor Adam Bruckner. As the first professor I met in the University of Washington Department of Aeronautics and Astronautics, he expresses his genuine care and love toward his students through every lecture and conversation. I could not build a solid foundation and experience the joy of swimming in the knowledge of the engineering field without him for the past four years.

Finally, I would like to thank Jesus for providing me an amazing church family and friendships in Seattle. Being a university student for six years, I could not grow so much without the full support and love from these people: David and Laura Chery, Brian and Maile Schneider, Ken and Grace Yang, Steve and Shuhui Morgan, Daniel and Yan Lu, David Bieraugel, Gabe Chan, Andrew Chen, James and Erica Chidester, Matt and Anna Randall, Jess Spence, Aaron and Rachel Wang, Reuben Straus, Brenton Ho, Kevin Choi, Roger Cheng, Drew Kang, Alexis Harroun, Grace Kim, Dzung Tran, Rostyslav Svitelskyi, David Lin, Ming Zhong, Noemie Nakamura, Andrew Abney, Jeff Engle, Joseph Lloyd. I love you all three thousand!

DEDICATION

To mom

Chapter 1
INTRODUCTION

1.1 Motivation

With the growing demand for space technologies and the persistent pursuit of scientific discoveries, the launch rate of hardware to space and other planets is rapidly rising. Landing a large payload on a planet surface will be essential for future expansion. Traditionally, parachutes are used to decelerate relatively light vehicles through the atmosphere. As the payload becomes heavier, ballistic coefficient, described by Eq. 1.1, is increased. Atmospheric entry consists of a high energy phase and a low energy phase [1]. The ballistic coefficient value determines if an atmospheric entry vehicle is capable of passively transition from high to low energy phase [1]. During the high energy phase, the entry vehicle travels at hypersonic speed. The kinetic energy is converted to heat due to atmospheric drag. In the low energy phase, the vehicle velocity is low enough, so that more traditional forms of deceleration, such as parachutes can be used.

$$\beta = \frac{m}{C_D A} \tag{1.1}$$

Mars landing is notoriously difficult due to its thin atmosphere. To date, all Mars missions have been robotic. The entry, descent, and landing (EDL) technology has been relying on similar types of hardware since the Viking missions [2]. During the high energy phase, the deceleration is achieved solely through the use of a heat shield. The ballistic coefficient is low enough for these types of spacecrafts to passively transition to low energy phase, which is mission critical. Then, hardware such as a supersonic disk-gap-band (DGB) parachute was deployed followed by subsonic propulsive terminal descent that would bring the vehicle to a soft touch-down.

As the ballistic coefficient increases, the vehicle may not passively reach the low energy

phase before reaching the ground [1]. Successful past Mars robotic missions' EDL trajectories are plotted and compared with a simulated Apollo command module Mars entry trajectory in Fig. 1.1. The ballistic coefficient of each vehicle is listed next to their names, and the low energy phase of the EDL is represented by a small box at the lower left of the graph. Having a ballistic coefficient significantly higher than the past robotic missions, 330 kg/m^2, an Apollo command module size vehicle would never reach the low energy phase relying solely on the Martian atmospheric drag.

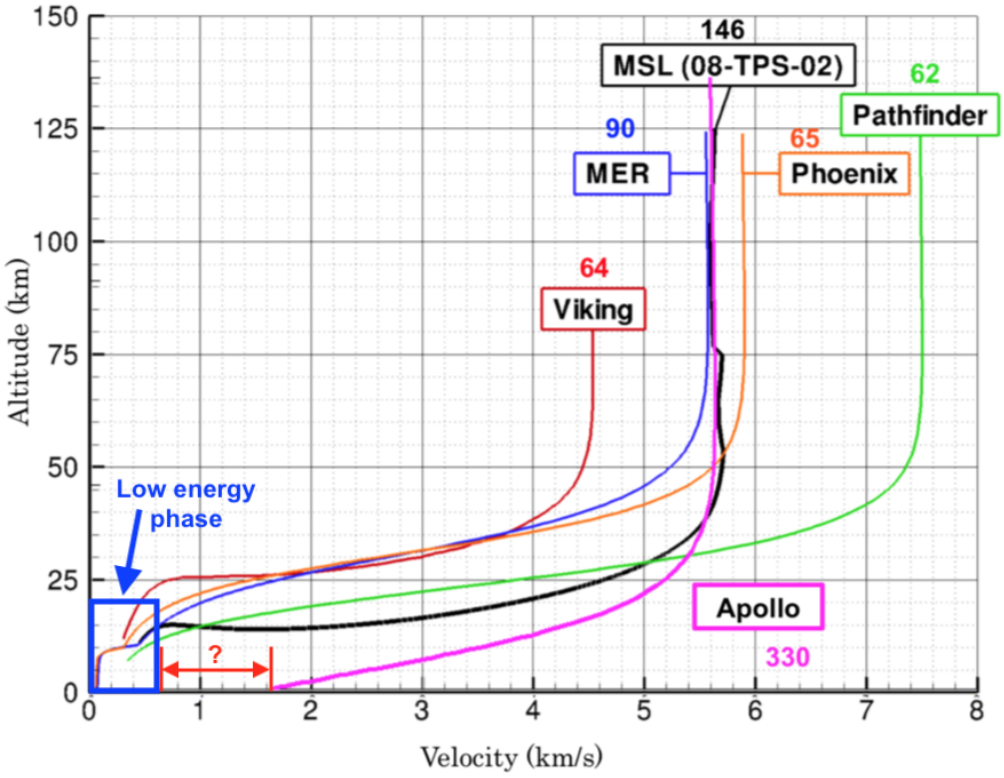

Figure 1.1: Simulated Apollo command module Mars entry trajectory in comparison with previous successful robotic missions with their ballistic coefficients listed [kg/m^2] [1]

An alternative method for EDL is required for a crewed vehicle to land on Mars. Supersonic retropropulsion (SRP) has been identified as one of the most promising methods

of landing large payloads on Mars. SRP is the method of firing engines into the oncoming supersonic or hypersonic flow, significantly slowing the vehicle in the high energy phase and allowing transition to the low energy phase [2]. Compared to the traditional EDL, implementing SRP has the benefit of reducing overall EDL system complexity by using the same engines for terminal descent, eliminating the need of parachutes [1]. In addition, a powered descent significantly increases control authority through the descent trajectory and hence landing precision [1].

Earth has a much thicker atmosphere than that on Mars, however, returning a rocket booster to Earth posts a similar challenge to Mars landing. Rockets inherently obtain high ballistic coefficients to minimize the drag losses during ascent. On the descent, high ballistic coefficients can lead to high heat loading that may compromise the vehicle. SpaceX, the only corporation to have successfully recovered orbital class boosters to date, utilizes SRP re-entry burn to minimize aerodynamic heating while providing active control for landing site targeting.

Even though SpaceX has successfully employed SRP technology, the lack of understanding of SRP flowfield characteristics has prevented this method of being used more widely. Accurate prediction of SRP conditions is even more critical for interplanetary missions such as Mars landing. Experimental and simulation data under a wide range of flow conditions is needed. Significant questions yet to be answered include, but not limited to:

- What is the best way to preserve the aerodynamic drag component at low thrust regimes to maximize efficiency and minimize propellant usage?
- How geometric and flow properties influence the flow regimes?
- How do we predict the configurations and flow regimes that lead to flowfield unsteadiness?

SRP flowfield unsteadiness is the phenomenon to be avoided and has many adverse effects include increasing structural loading due to vibrations, higher heat loading, and compro-

mising control authority due to poor predictions. Investigating the unsteadiness of SRP flowfields is the main focus of this thesis. A study of the effect of jet pressure, as a proxy for thrust coefficient, on flowfield topology and unsteadiness of multi-nozzle SRP configurations, is presented.

1.2 Problems and Goals

The interactions between retro-nozzle jets and incoming supersonic freestream create many unique SRP flowfield features. Fig. 1.2 is an example of a single, central, under-expanded jet configuration SRP flowfield with key features labeled. The bow shock is pushed forward by the jet. The shock standoff distance increases with increasing jet mass flux [3]. The jet and the freestream interact in front of the forebody. Along the center line, from left to right, the flow velocity is changed from freestream supersonic to subsonic through the detached bow shock. The flow direction reverses after a free stagnation point and then is supersonic again on the jet side of the jet terminal shock. Due to the significant change in flow directions, circulation regions are formed around the central jet [2].

Flowfield topology does not necessarily appear to be similar to Fig. 1.2. Studies have shown that SRP flowfield features heavily depend on jet pressure. Daso et al. (2007) both experimentally and numerically demonstrated that as the jet pressure or jet thrust increases, the flowfield often transitions from steady to unsteady then back to steady [3], shown in Fig. 1.3. Jet penetration through the bow shock is associated with an unsteady SRP flowfield. Large bow shock movement is present in the penetrated region, causing the bow shock boundary to disperse.

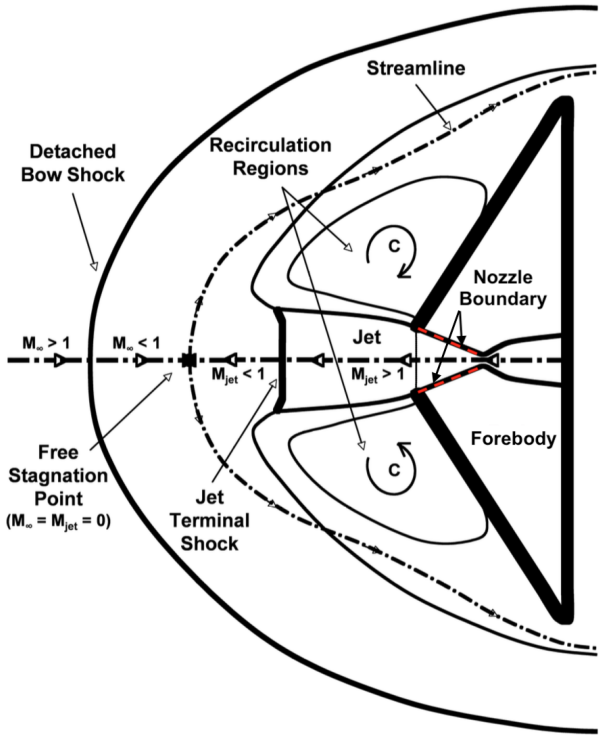

Figure 1.2: Flowfield of a center nozzle configuration on a forebody with key features labeled [2]

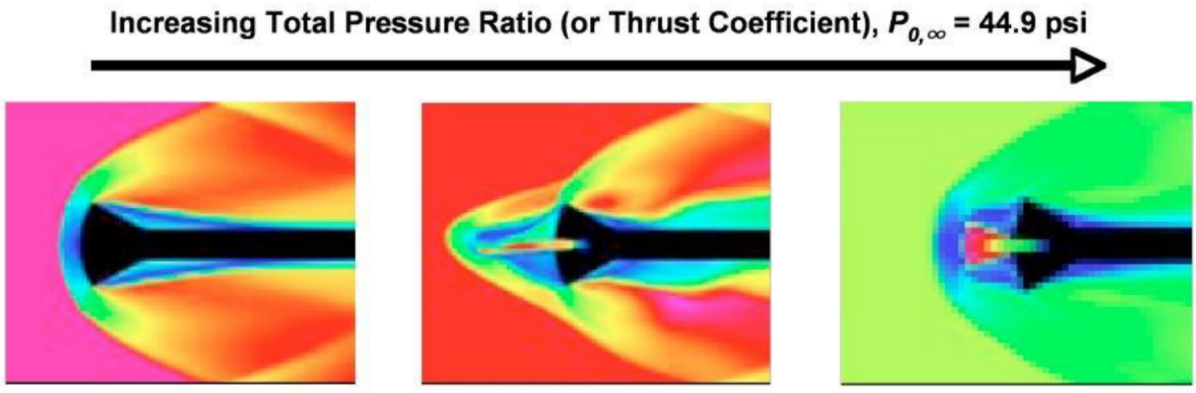

Figure 1.3: Simulation of central nozzle SRP flowfield transitioning from stable to unstable then back to stable as thrust coefficient increases [3]

SRP flowfield unsteadiness has previously only been associated with the jet penetrating the bow shock. The jet extending into the far upstream of the freestream and disrupting the smooth bow shock curvature is known as a long penetration mode (LPM) [3]. The LPM mostly occurs at low jet expansion ratios, where the jet is perfectly or near-perfectly expanded. A small jet with a large forebody is likely to promote LPM as well. The SRP flowfield becomes unsteady as the bow shock being disrupted that it is no longer fixed at the same location over time [3].

Recently, it was discovered by Tan (2018) that unsteadiness could occur without the penetration of the bow shock when the jet and the freestream have equal stagnation pressures [4]. Periodic oscillatory motion of the entire shock was observed. The extent of the bow shock movement is shown in Fig. 1.4. The geometry of the bow shock remains similar at the forward-most and the backward-most positions, and the smooth curvature of the shock front is preserved throughout. Tan (2018) observations leave hypothesis for more types of unsteadiness to investigate. Much more studies could be done on the prediction of unsteadiness.

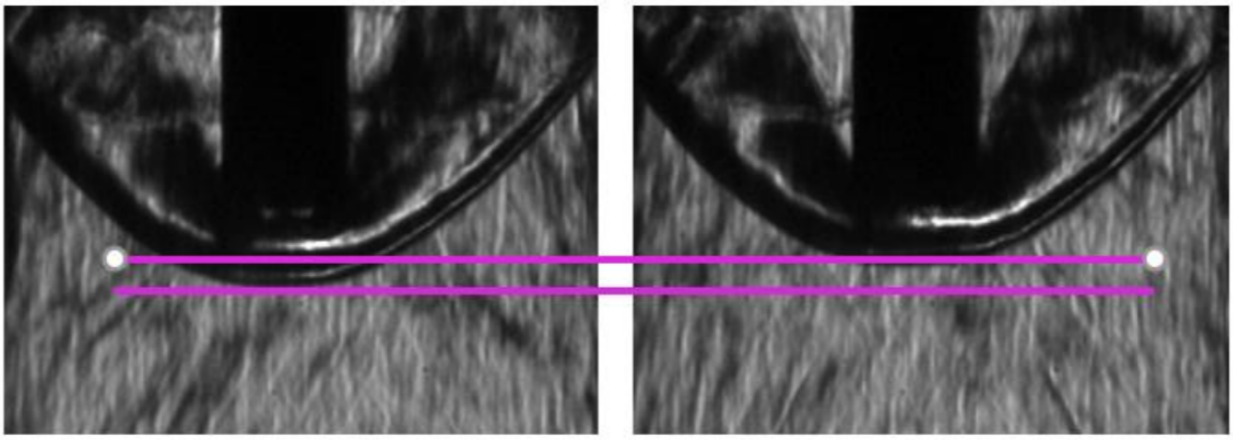

Figure 1.4: Bow shock oscillating magnitude for $P_{0j}/P_{0\infty} = 1$, no shock penetration appearing [4]

Tan (2018) studied a single nozzle configuration without a forebody. Many envisioned SRP applications often involve multiple engines firing into the freestream. In some cases, firing multiple engines helps save propellant by reducing burn time, thus reducing gravity losses. In other cases, arranging the engines peripherally on a forebody enlarges the bow shock to preserve a large area of high pressure on the body, an therefore preserves a large component of natural aerodynamic drag. The efficiency of SRP can be increased as a result [2]. When multiple jets are present, they interact both with each other and freestream. Fig. 1.5 presents a scenario for three highly under-expanded jet. Depending on the expansion ratio, jets can impinge on each other while matching the pressure of ambient conditions. Little studies have done on interactions among jets, and it can be further investigated.

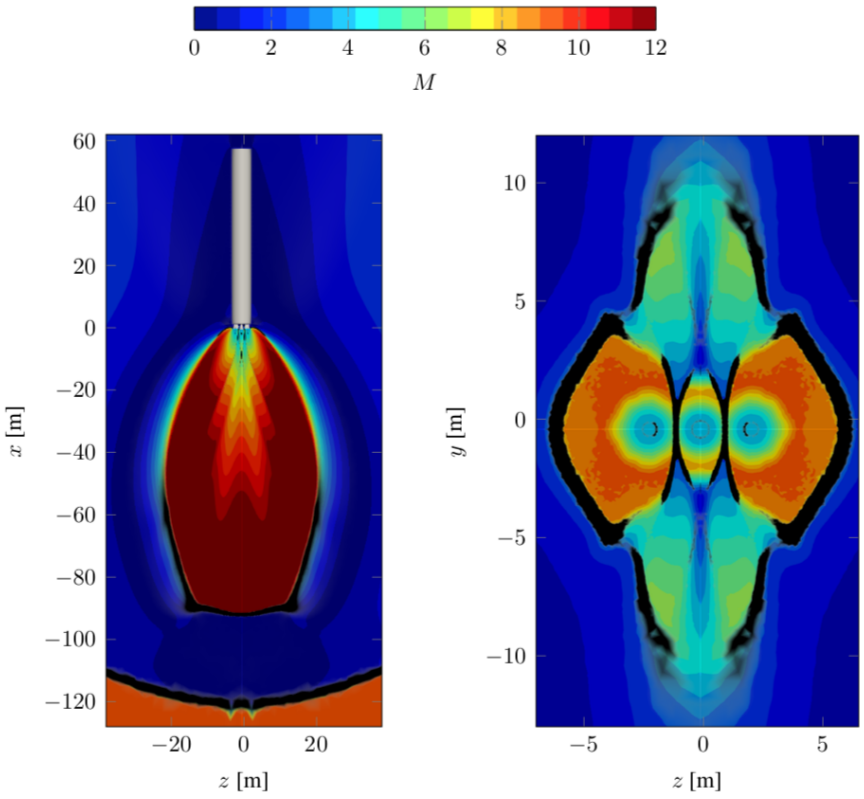

Figure 1.5: Highly under-expanded jets interaction in a SRP flowfield [5]

This thesis experimentally studies the influence of jet pressure on multi-jet configuration and flowfield unsteadiness with these goals:

1. Compare a tri-nozzle flowfield topology to a range of single-jet configurations.

2. Examine the three-dimensionality of the tri-nozzle flowfield.

3. Determine the conditions ($P_{0,ratio}$) under which the tri-nozzle flowfield is unsteady, as well as classify the unsteadiness.

These goals were achieved experimentally using a Mach 2 Ludwieg tube and schlieren photography. An inline tri-nozzle similar to the Falcon 9 reentry burn configuration was fabricated. Each nozzle interior is geometrically similar to the retro nozzle used by Tan (2018). A schlieren system was developed to capture the SRP flowfield with shorter exposure time and more consistent background intensity compared to Tan (2018) data. Mean and RMS fields of the stabilized videos were extracted to qualitatively examine changes to bow shock topology, standoff distance, shock motion, and configuration with increasing jet pressure. It was found that two types of unsteadiness, bow shock oscillation, and bow shock penetration, both occur at the same jet-to-freestream stagnation pressure ratio, independent of nozzle geometry.

Chapter 2

BACKGROUND & THEORY

2.1 Aerodynamic Drag Loss

There are two dominant forces contribute to the deceleration of an SRP vehicle, aerodynamic drag and thrust. The total axial force coefficient is defined as the sum of C_D and C_T, shown in Eq. 2.1, where C_D and C_T are the non-dimensional drag and thrust coefficients. They are non-dimensionalized by the product of dynamic pressure, q and forebody area, A.

$$C_A = C_D + C_T \tag{2.1}$$

The drag coefficient is heavily dependent on the thrust coefficient. For a single nozzle located at the center of a forebody, an increase in thrust coefficient leads to a decrease in drag coefficient [2]. One measure of SRP efficiency is the proportion of the total force that comes from aerodynamic drag. This is seen to reduce with increasing thrust coefficient. Fig. 2.1 [2], demonstrates the decrease in C_D caused by increasing C_T. At C_T =0, the C_D at different Mach numbers have values between 0.6 and 0.8 for the example capsule-like geometry. At C_T = 1.5, C_D could be as low as 0.2. It is clearly presented in Fig. 2.1 that for M_∞ = 4.5, as the C_T increases from 0 to 0.5, it is possible for C_A to even decrease for small C_T relative to having no SRP at all. Adding a retro-jet may cause the vehicle to slow down less quickly [2]. For efficiency and overall effectiveness, it is important to investigate methods for preserving the aerodynamic drag on SRP vehicles. The use of multi-nozzle configurations has been shown to help accomplish this goal.

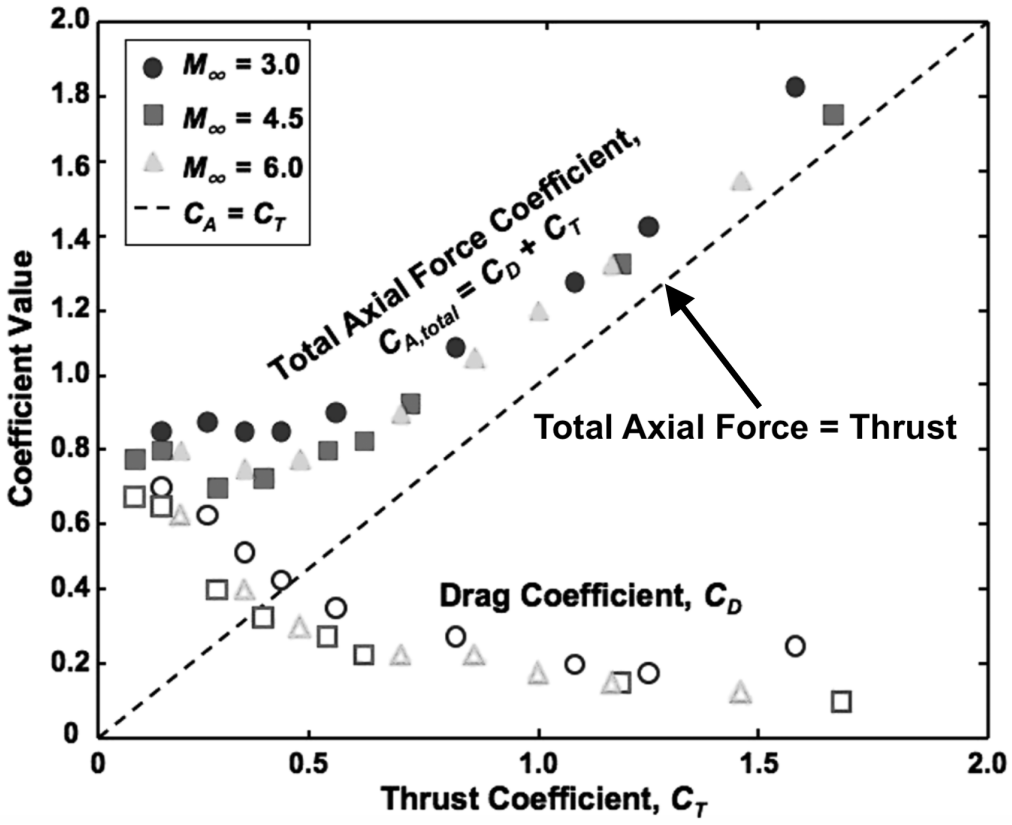

Figure 2.1: Variation of drag coefficient due to increase in thrust coefficient for a simple forebody with a single, central nozzle arrangement [2]

Previous studies have shown that arranging multiple nozzles peripherally on a forebody instead of centrally would help preserve the drag as the thrust increases [2]. In Fig. 2.2, the difference in the total axial force coefficient is compared between the central configuration and the peripheral configuration. As the peripheral nozzle configuration preserves a greater component of aerodynamic drag, the engines can operate at a much lower C_T, or lower jet pressure, to achieve the same axial force requiring more than double the C_T for the central nozzle case. The significant benefit of drag preservation gained by multi-nozzle configuration highlights the importance of understanding multi-nozzle SRP flowfields at various regimes.

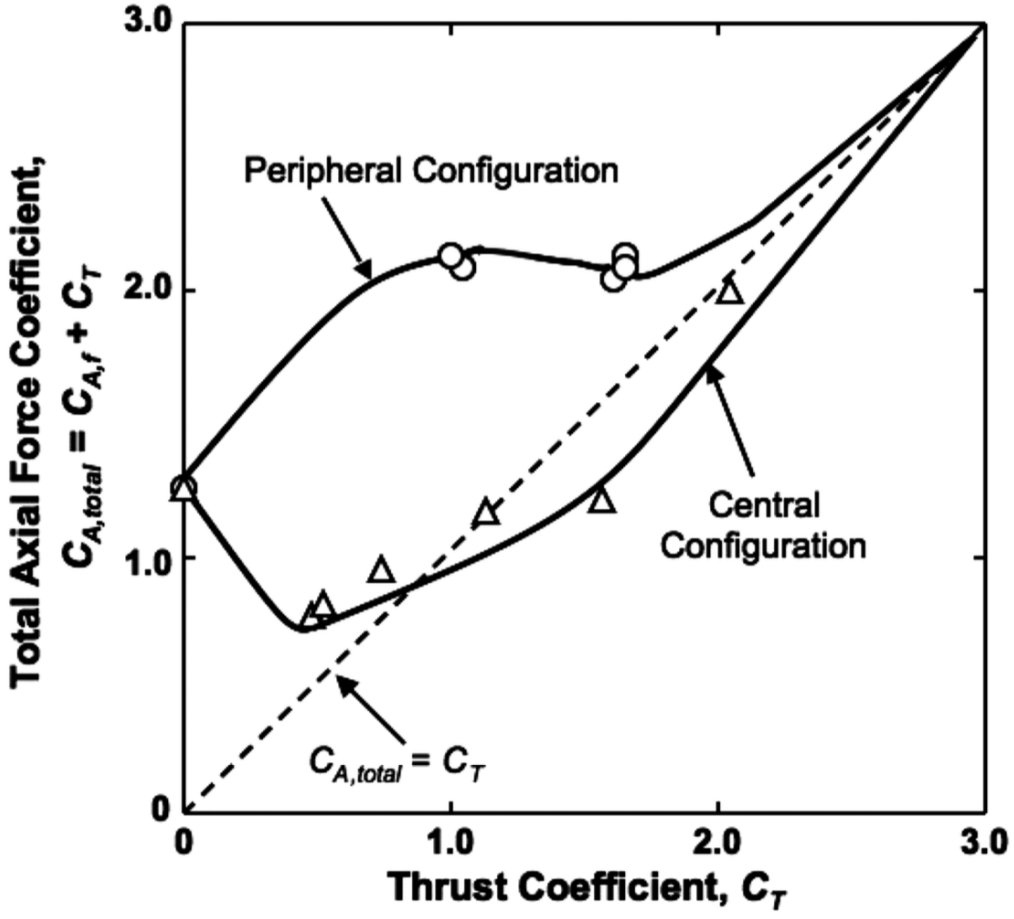

Figure 2.2: Axial force difference between central nozzle configuration and peripheral nozzle configuration due to difference in drag preservation [6]

2.2 Basic SRP Flowfield Features for Single and Multi-nozzle Configurations

SRP for central and peripheral nozzle arrangements were studied by Korzun et al. (2009). Example flowfields of each nozzle arrangement is presented in Fig. 2.3.

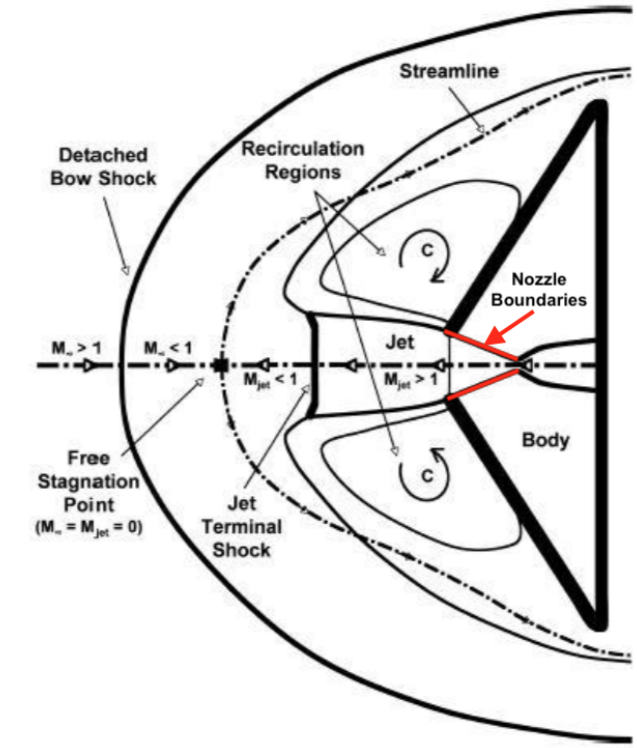

(a)

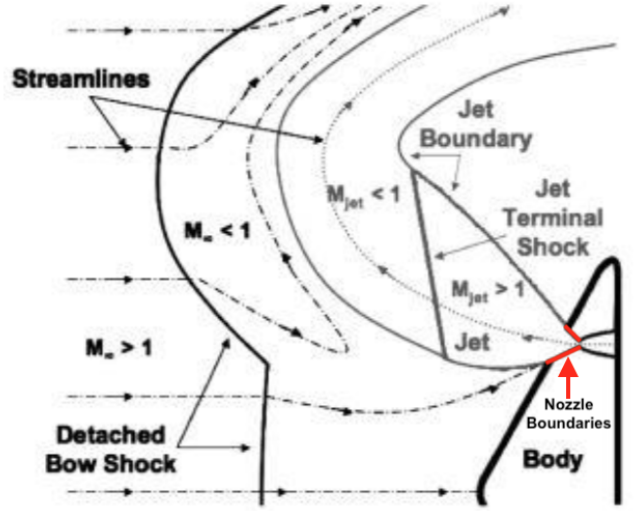

(b)

Figure 2.3: Flowfield features of the center nozzle configuration (a), and peripheral nozzle configuration (b) [2]

In Fig. 2.3, flowfields for an underexpanded single central and peripheral nozzle are compared. The central jet can lead to a reduction in bow shock curvature. This can lead to a reduction in base pressure and thus less aerodynamic drag. The general SRP flowfield features of peripheral nozzle configuration are shown in Fig. 1.2 (b). The exhaust is swept away from the forebody, without creating recirculation regions that separate the forebody from the freestream. Inboard of the retro-nozzles, the bow shock is much less disturbed compared to the central nozzle case. As a result, the central portion of the body sees a flow very similar to that which it would see without the retrojet present. The entire bow shock is also enlarged by the peripheral jets, leaving a greater footprint in the flow. These factors all contribute to the preservation of the aerodynamic drag component while enhancing the total force on the body.

SRP flowfields of an inline tri-nozzle on a forebody are studied. This configuration is easy to interpret using schlieren photography and similar to the re-entry burn configuration of a Falcon 9 first stage booster, which is a multi-nozzle configuration that has flown. The geometry of the Falcon 9 first stage booster is shown in Fig. 2.4, three of the nine engines are used. In Fig. 2.5, three-dimensionality of the Falcon 9 SRP flowfield is shown in a highly underexpanded configuration. The study of Eker et al (2017) focused on the operational envelope of the Falcon 9. The bow shock appears to be wider in the direction perpendicular to the tri-nozzle lineup. This directional asymmetry is caused by highly underexpanded jets impinging on each other.

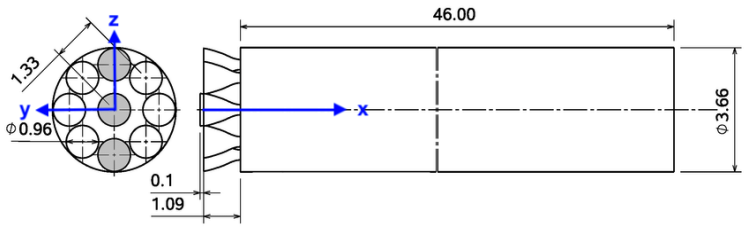

Figure 2.4: Simplified Falcon 9 first stage geometric specification, and the triple nozzle inline with z-axis are the ignited engines. [7]

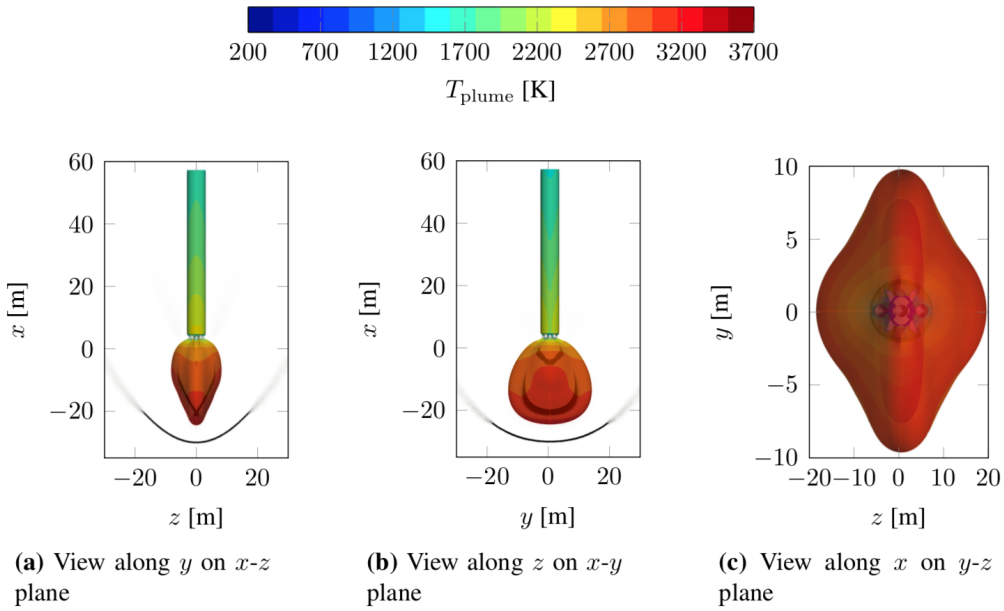

(a) View along y on x-z plane

(b) View along z on x-y plane

(c) View along x on y-z plane

Figure 2.5: Simulation of Falcon 9 first stage reentry burn at 37 km altitude, Mach 5.09 [8]

2.3 Jet Expansion

So far, the SRP flowfields have only been discussed for highly underexpanded jets but the expansion ratio of engine nozzles or the atmosphere or altitude of various SRP vehicles may result in a range of jet expansion patterns, some of which are known to be unstable. Jet expansion pattern is influenced by the jet exit pressure to ambient pressure ratio, P_j/P_a. Fig. 2.6 presents three general patterns of a jet. If the ratio is smaller than one, the jet is over-expanded. If the ratio is greater than 1, the jet is under-expanded. The shock-expansion fan patterns allow the jet to pressure to match its surroundings. Under-expanded jets generally carry more momentum than over-expanded jets. For an over-expanded jet, an oblique shock can be observed appearing on the lip of the exit plane, turning the lower pressure jet inward. A mildly under-expanded jet would be turned outward through an expansion fan emanating from the nozzle tip. For the case of a highly under-expanded jet, the jet static exit pressure is so high that the abrupt change in pressure leads a normal shock to form, intersecting a

barrel shock and a reflected shock on the triple point.

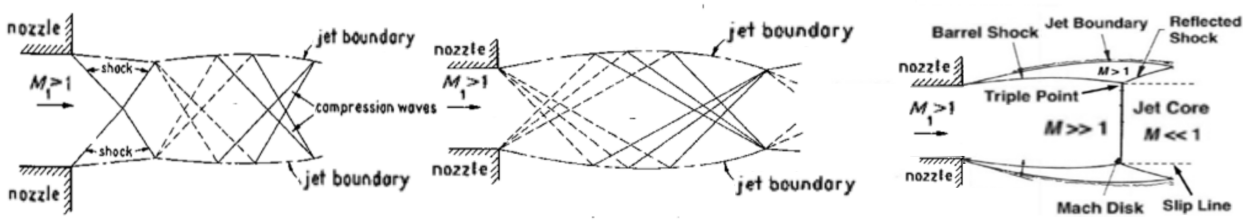

Figure 2.6: Jet expansion pattern into a quiescent medium: over-expanded (left), mildly under-expanded (middle), highly under-expanded (right)[9]

2.4 SRP Flowfield Steadiness Regimes

Accurate prediction of SRP flowfield unsteadiness is critical due to its potential impact on stability, control, vehicle loading, and heat transfer. Regimes of stability have been previously classified are mostly classified based on the motion or disruption of the bow shock. The standoff distance, oscillatory motions, and penetration by the opposing jet are the key features of classification. It has been observed that for a central nozzle configuration, as the thrust coefficient increases, the flowfield transitions from stable to unstable, and then back to stable [2, 3, 15]. The short penetration mode (SPM) is considered a steady flowfield, where the retro jet is either over-expanded or highly under-expanded. This mode does not affect the smooth bow shock topography [3]. Jet expansion and shock waves with the bow shock appear to be blunter. The long penetration mode (LPM) is an unstable or unsteady flowfield where the jet punches through or penetrates the bow shock. This sometimes occurs when the jet is perfectly or moderately under-expanded. Jet momentum could be carried over a long distance due to a less energy loss through weaker shocks with shallower angles. Weaker strengths on the shock results in oscillation of shock structure because the shock structure is more oblique as the jet penetrating. For LPM, the bow shock is highly dispersed, and the standoff distance is difficult to determine [3].

Conducted by Jarvinen and Adams (1970), a triple nozzle SRP arranged peripherally

on a 60 degree-aero shell are shown in Fig. 2.7 left picture. It was found that (stated by Korzun et al.) the sudden increase of shock standoff distance and dissolution of the bow shock occurred for central nozzle retropropulsion was not found for triple nozzle peripheral configuration [2, 10]. The unsteadiness for multi-nozzle configurations involves the portion of the bow shock inboard of the nozzles being disturbed by the jet flows. Similar studies on a 70-degree aeroshell forebody with three peripherally configured nozzle have been conducted by Berry et al. (2011) [11], and later Berry and Rhode (2014) [16]. The triple nozzles were placed more inboard, and the angle of the aeroshell cone is 10-degree larger compare to Jarvinen and Adams (1970) apparatus, shown in Fig. 2.7 right picture. Unsteady LPM was observed by Berry et al. (2011) testing in Langley Unitary Plan Wind Tunnel [16]. Jet plumes independently protrude through the bow shock at the lowest thrust coefficient ($C_T = 0.5$) [16]. A comparison of Jarvinen and Adams (1970) and Berry and Rhode (2014) studies, the unsteadiness of multi-nozzle SRP is not well classified. Jarvinen and Adams (1970) did not specify if LPM appeared in the unsteady regime, while Berry and Rhode (2014) indicated the appearance of LPM unsteadiness. Current definitions of unsteadiness regimes are not complete.

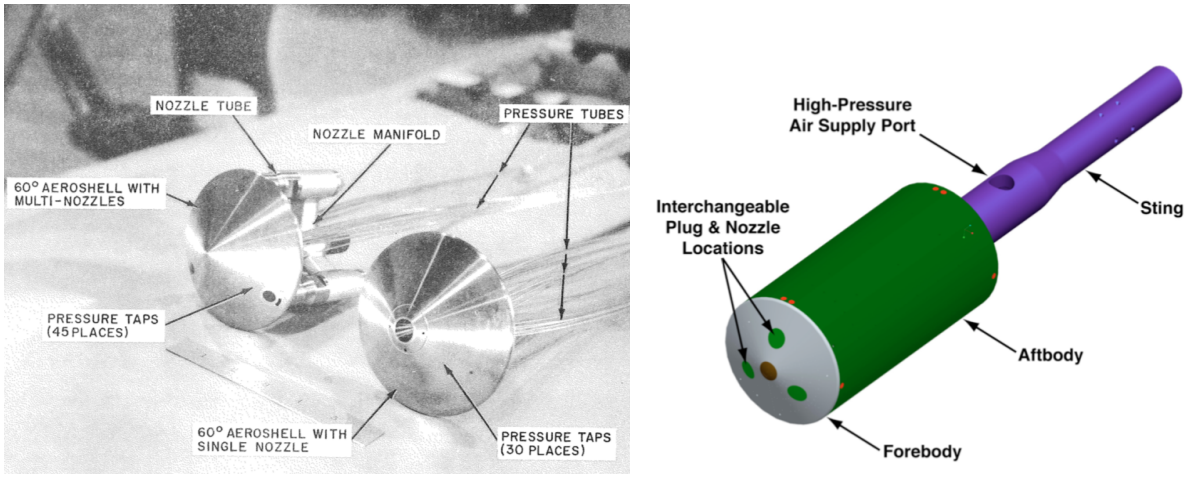

Figure 2.7: Left picture: 60-degree aero shell apparatus tested by Jarvinen and Adams (1970) [10]. Right picture: 70-degree aero shell forebody tested by Berry et al. (2011) [11]

It was suggested by Tan (2018) study, the unsteadiness of SRP flowfield is a result of multiple mechanisms. LPM is not required for unsteadiness [4]. It was observed that for a single nozzle without a forebody, the entire shock oscillates without significant deformation when the opposing jet is near-perfectly expanded [4]. An example of this motion is shown in Fig. 1.4. As a continuation of Tan (2018), the unsteadiness characteristics of an inline tri-nozzle that is geometrically comparable to Tan (2018) apparatus is studied. A range of single-jet geometrically similar to the jet conducted by Tan (2018) was tested to ensure that the unsteadiness observed by Tan was not a result of the scale of the apparatus.

SRP flowfields of an inline tri-nozzle configuration are investigated in this thesis. This arrangement has been used by SpaceX for the first landing of an orbital class booster. Placing three nozzles inline enables cleaner interpretation of schlieren photography than peripheral arrangement. Inline tri-nozzle configuration was studied by Zilker (2018) in the flow regimes of Falcon 9 first stage booster at reentry burn altitude range [5], involving mostly stable, highly under-expanded jet flows. Aerothermal analysis based on steady Reynolds Averaged Navier Stokes (RANS) simulation was done. However, the characteristics of unsteadiness of this multi-nozzle configuration are yet to be explored.

Chapter 3

EXPERIMENTAL APPARTUS & METHODS

3.1 Ludwieg Tube

A 7.62 cm (3 in) inner diameter Ludwieg tube with a 3-meter long driver section was used as a Mach 2 supersonic wind tunnel to produce approximately 16-millisecond steady supersonic freestream nitrogen flow in the open air. Fig. 3.1 presents the experimental set up of the Ludwieg tube. The driver section was filled by one compressed nitrogen bottle as a reservoir. A Mach 2 waveless nozzle was attached downstream of the driver section. Between the nozzle and the driver section, a double diaphragm breech was used as a fast opening valve to start the Ludwieg tube. The retro-nozzle assembly was located on the center line of the Ludwieg tube, downstream the Mach 2 waveless nozzle. The parabolic mirror was a part of the schlieren system for flow visualization. The recoil bumper was installed to fix the Ludwieg tube in position. An Omega PX309 pressure transducer was used to monitor the driver section reservoir pressure.

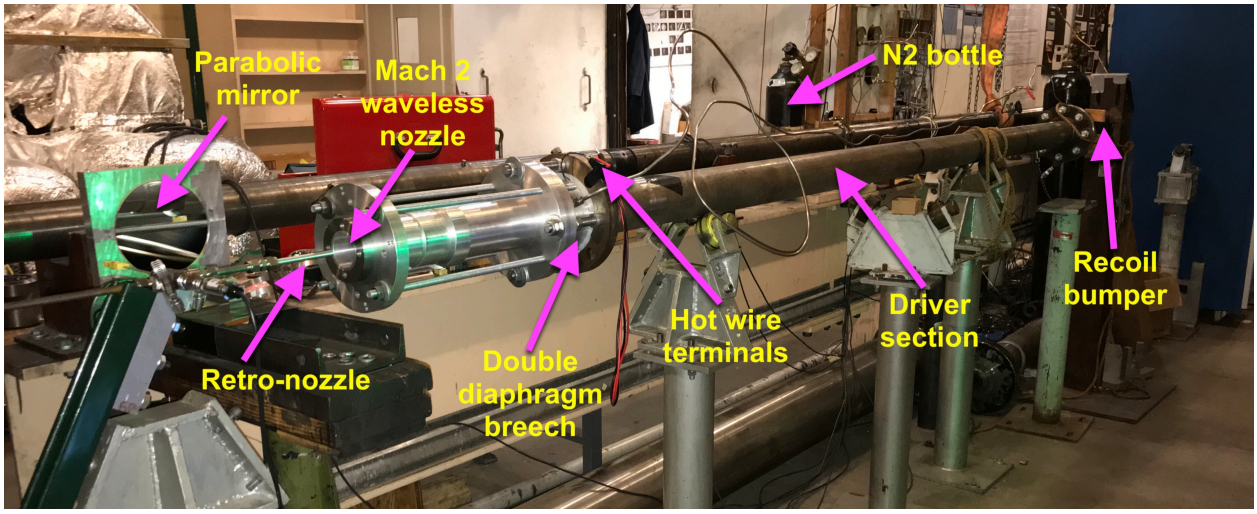

Figure 3.1: The Ludwieg tube used as a supersonic wind tunnel

A schematic of the Ludwieg tube operational principles is illustrated as a t-x diagram shown in Fig. 3.2. The gas is stationary in the driver section and is used as a reservoir, with pressure, temperature, and density noted as p_{Res}, T_{Res}, and ρ_{Res}. A diaphragm is located downstream of the driver section and upstream the supersonic waveless nozzle, isolating the driver section reservoir conditions from the pre-start downstream conditions. The Ludwieg tube is started by bursting the diaphragm. A shock and expansion fan emits from the diaphragm location. Region 3 is the portion where the gas is accelerated by the expansion fan. Downstream region 3, before the gas reaching the supersonic waveless nozzle divergent portion, the converging portion of the nozzle causes a change in entropy and establishes new stagnation conditions through the nozzle noted as p_s, T_s, and ρ_s. Once the new stagnation conditions are established, the flow is expanded isentropically to supersonic velocity into the test region. For the Ludwieg tube used in this thesis, the test region is located in open air. The approximate location of the test region is indicated as region 2. The static pressure of the fully established supersonic flow in region 2 is necessary to match the ambient pressure of the lab to produce a perfectly expanded supersonic flow. The stationary ambient air is indicated as region 1.

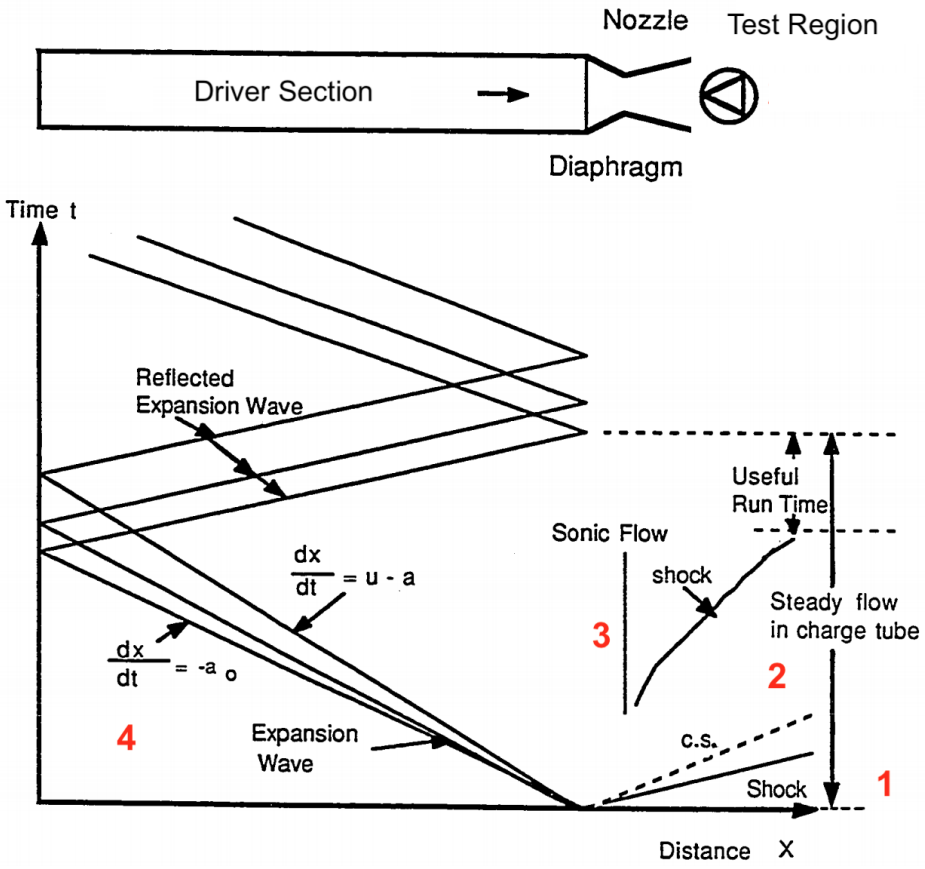

Figure 3.2: Ludwieg tube t-x diagram for an upstream-throat diaphragm [12]

The new stagnation conditions through the supersonic waveless nozzle are functions of nozzle throat-to-tube area ratio only. The pressure and temperature change as a result of area ratio is shown in Fig. 3.4. As the throat of the nozzle gets bigger, the difference between the new stagnation conditions and the reservoir conditions becomes larger. To avoid large change of the stagnation pressure and temperature from the reservoir conditions to the new stagnation conditions, the nozzle throat-to-tube area ratio is more desirable to be small. The Mach 2 waveless nozzle used in this thesis is shown in Fig. 3.3. This particular nozzle has a nozzle throat-to-tube area ratio of 0.27, keeping the new stagnation pressure to reservoir pressure ratio above 0.8, as the red vertical line shown in Fig. 3.4.

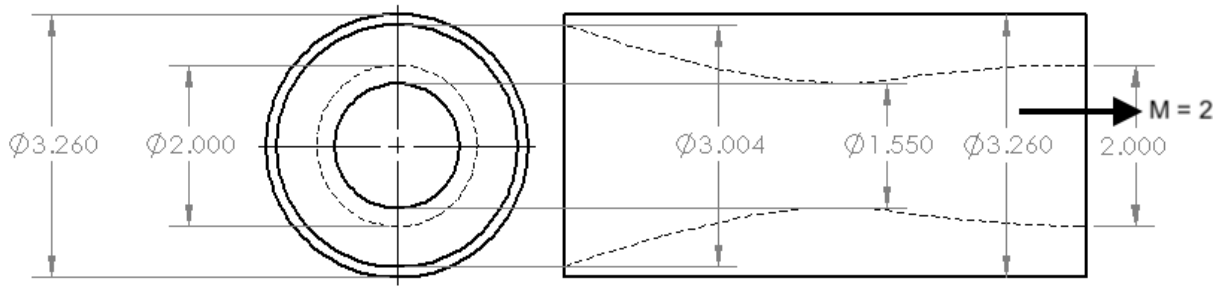

Figure 3.3: The Mach 2 waveless nozzle used in the Ludwieg tube

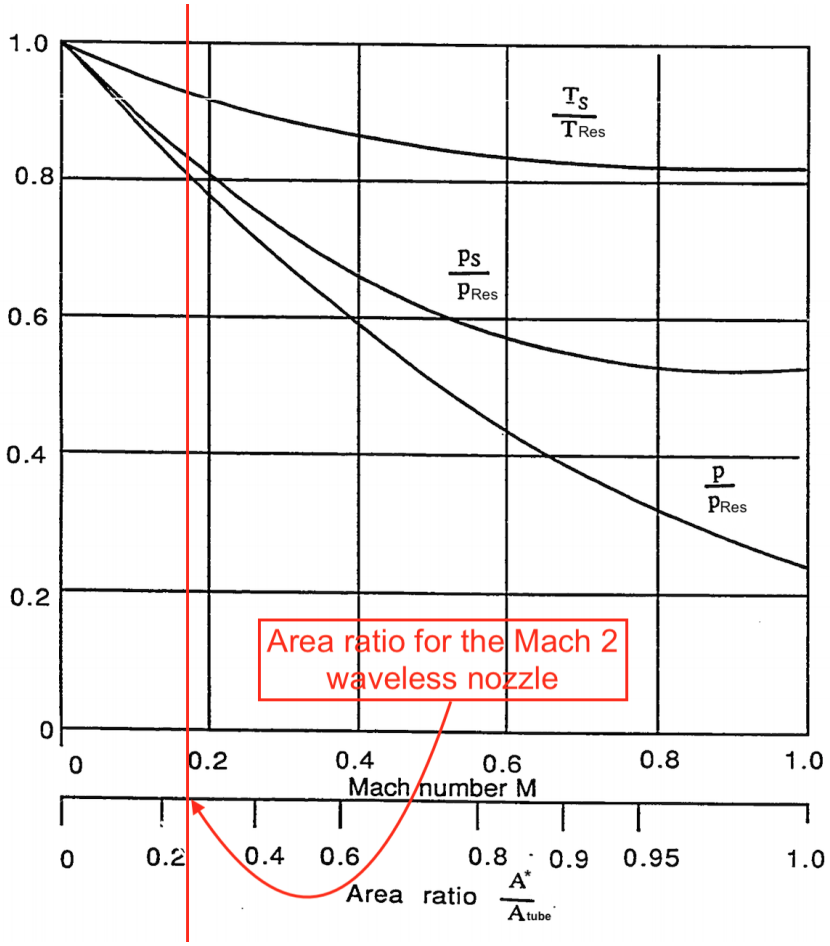

Figure 3.4: Pressure and temperature ratios vs. area ratio [12]

The Mach number just before the nozzle convergent section is a function of throat-to-tube area ratio only [12], can be expressed as

$$\frac{A_{tube}}{A^*} = \frac{1}{M}(\frac{1+\frac{\gamma-1}{2}M^2}{\frac{\gamma+1}{2}})^{\frac{\gamma+1}{2(\gamma-1)}} \tag{3.1}$$

Stagnation-to-total temperature ratio and sonic speed ratio can be determined using the Mach number just before the nozzle convergent section. Note that the subsonic value is used because region 3 is located upstream the choking point [12].

$$\frac{T_s}{T_{Res}} = (\frac{a_s}{a_{fill}})^2 = \frac{1+\frac{\gamma-1}{2}M^2}{(1+\frac{\gamma-1}{2}M)^2} \tag{3.2}$$

Through isentropic relations, pressure and density ratios can be solved through temperature ratio or speed of sound ratio [12].

$$\frac{p_s}{p_{Res}} = (\frac{a_s}{a_{Res}})^{\frac{2\gamma}{\gamma-1}} \tag{3.3}$$

$$\frac{\rho_s}{\rho_{Res}} = (\frac{a_s}{a_{Res}})^{\frac{2}{\gamma-1}} \tag{3.4}$$

The Ludwieg tube has an inner diameter of 3 inches. The Mach 2 nozzle has a throat diameter of 1.550 inches. Pre-supersonic nozzle Mach number can be solved using Eq. 3.1. Then applying Eq. 3.2, temperature ratio can be determined. Pressure ratio is calculated using isentropic relations for Mach 2 flow. In the following SRP experiment, the static pressure of the Mach 2 freestream is 14.7 psi, standard atmospheric pressure at sea level. Ambient-to-reservoir pressure ratio for this particular Ludwieg tube is calculated to be 0.1042, translating to 140.9 psia fill pressure, to produce a perfectly expanded Mach 2 flow into the ambient air.

A double diaphragm breech, shown in Fig. 3.5 that sits between the driver tube and the nozzle enables two types of diaphragm bursting modes: pressure burst and hot wire burst. Hot wire burst was used in the following experiments so that the Ludweig tube and camera could be triggered simultaneously. Single sheet 7.5-mil Mylar was sufficient to hold 140.9 psia gas pressure in the Ludwieg tube driver section. A piece of one inch long 36 gauge nichrome 80 wire was taped at the center of the diaphragm. A 40 A current was sent through the nicrhome wire and a TTL signal to Phantom V1211 high-speed camera were sent by a trigger box simultaneously. The camera was triggered just before the diaphragm burst due to nichrome wire heating, ensuring the full capture of the steady Mach 2 flow.

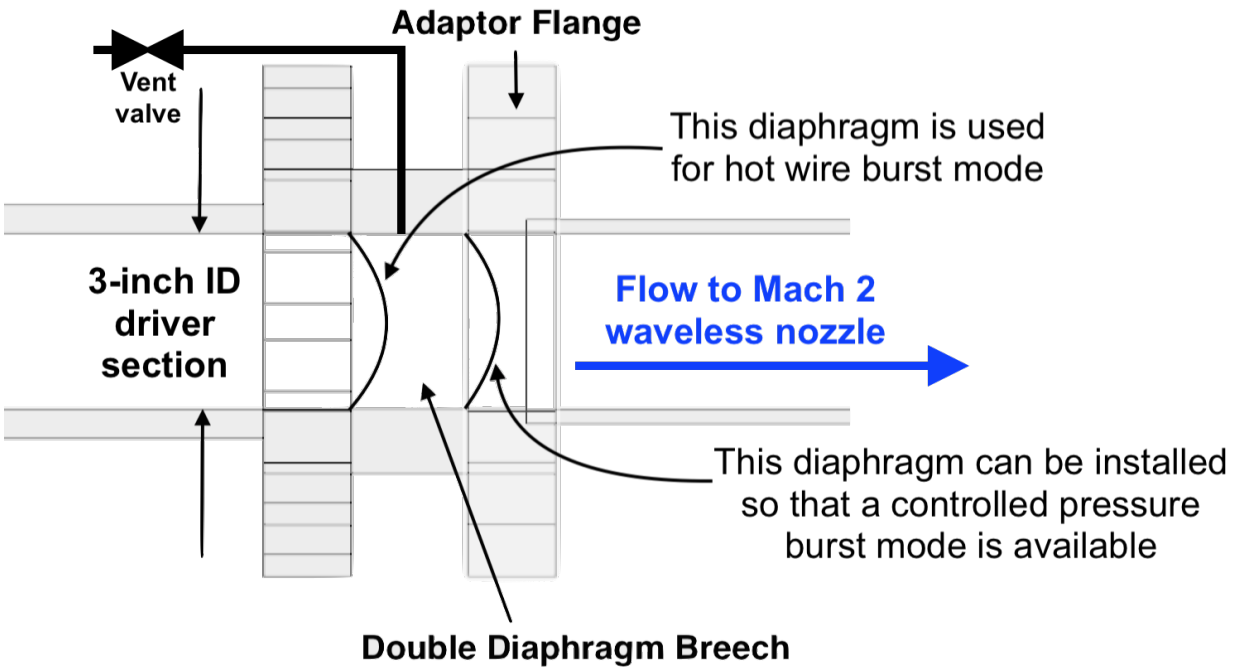

Figure 3.5: The schematic of the double diaphragm breech with two bursting modes available

3.2 Tri-nozzle Design and Verification

A miniature rocket forebody with three conical nozzles arranged inline was designed, shown in Fig. 3.6. The area ratio of each nozzle was designed to produce a Mach 2 nitrogen flow at

the nozzle exit. These nozzles are not waveless designs, instead, they are 4-degree half-angle cones for the ease of manufacturing. Constant stagnation pressure up to 600 psi was provided by three nitrogen cylinders via a pressure regulator. The stagnation pressure was monitored by an Omega PX309 pressure transducer located just upstream the retro-nozzle.

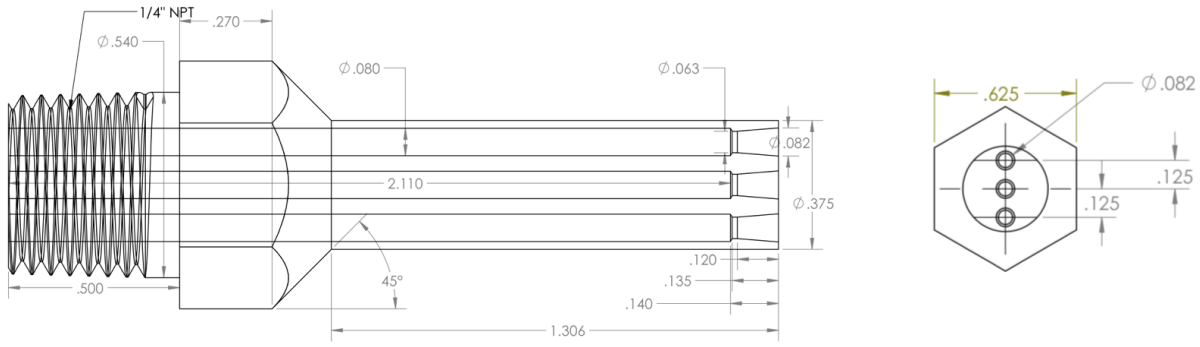

Figure 3.6: Tri-nozzle design drawing

To manufacture three identical Mach 2 conical nozzles on a small scale, a 4-degree half angle tool was made, so each nozzle would obtain the same divergent angle. A constant depth was drilled to create the same throat and exit areas. Any machine error could be magnified due to its small size. It was not possible using available equipment to examine the interior of any of the three small nozzles to verify the machining accuracy by direct measurement. Schlieren pictures of the tri-nozzle operating in quiescent air in two orientations were taken to verify if all nozzles could produce the same the jet structures with identical Mach expansions. Fig. 3.7 presents a time-average picture of the three retro-nozzle jets in the vertical orientation. Barrel shocks from each nozzle intersect at the same distance from the nozzle exit plane. Further downstream, the shock patterns in the exhaust appear to be symmetric. Fig. 3.8 presents a time-average picture of three retro-nozzle jets in the horizontal orientation. No out-of-plane jet can be observed in the picture. The supersonic jet structure appears to be symmetric and almost identical to that of a single jet. These two time-averaged images verify that these nozzles have the same area ratios and point in the

same direction.

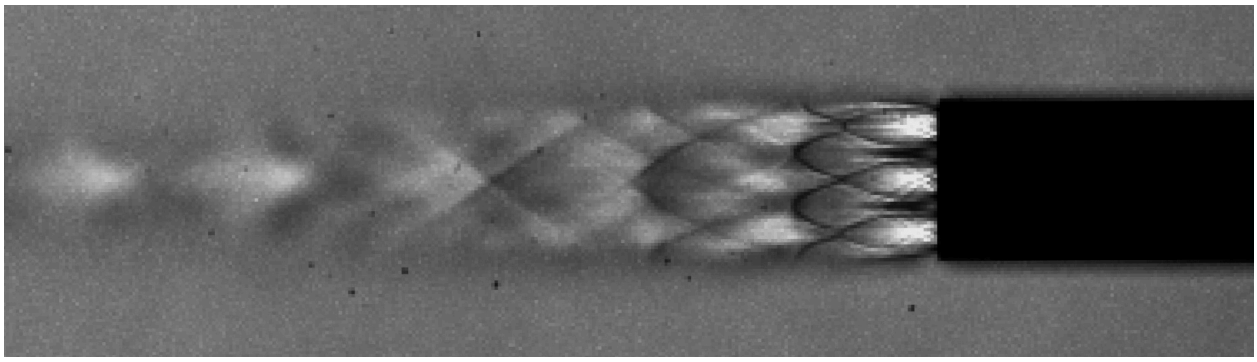

Figure 3.7: Under-expanded tri-nozzle jets, vertical view

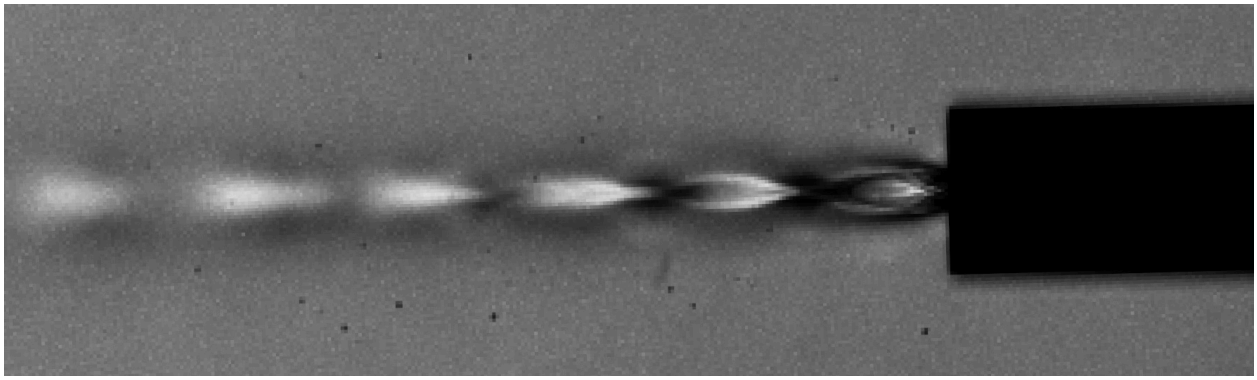

Figure 3.8: Under-expanded tri-nozzle jets, horizontal view

3.3 Comparison Nozzles

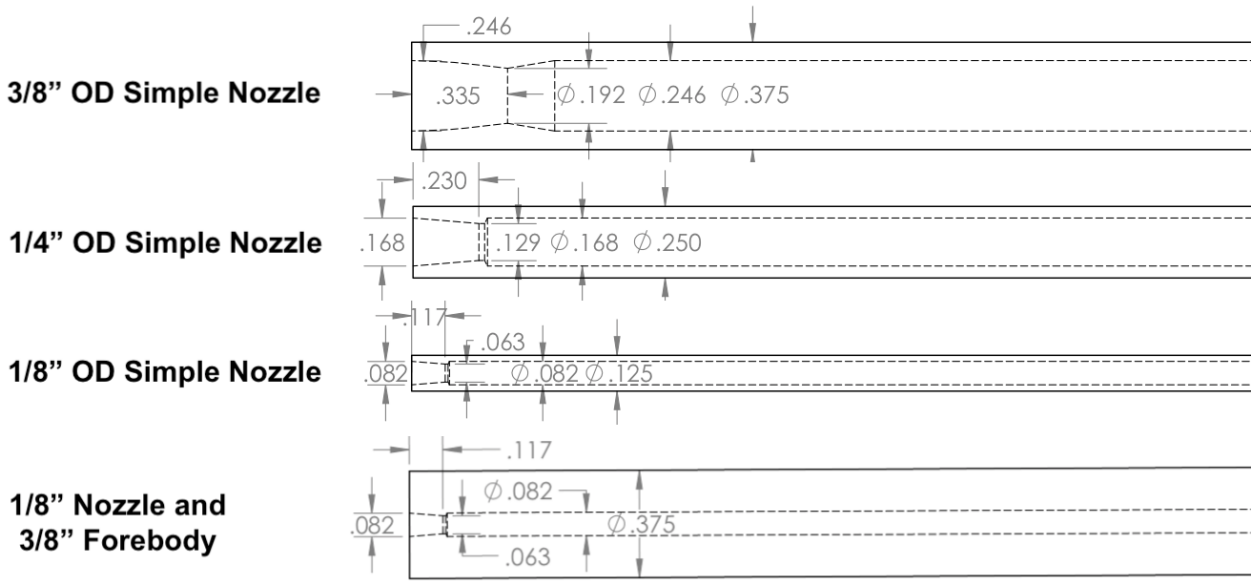

Figure 3.9: Dimensions of single nozzles used in the experiment

A range of single nozzle configurations were used for comparison with the tri-nozzle configuration. Critical dimensions of retro nozzles are presented by Fig. 3.9, note that the length of each nozzle is much longer than indicated here. 3/8" OD simple nozzle was studied by Tan (2018) and retested with the improved schlieren setup.

Chapter 4

DESIGN AND TEST OF THE SCHLIEREN SYSTEM INCORPORATING AN OVERDRIVEN LED LIGHT SORUCE

This chapter presents the design process and performance verification of the schlieren system used in the following experiment. A pulsed LED light source based on the design of Lincoln (2016) was manufactured and tested. The characteristics of the optical setup and the pulsed LED circuit were examined.

4.1 Optical Elements

Due to the lab space constraints, a single-mirror, coincident schlieren system was selected for supersonic retropropulsion flowfield visualization. The basic concept for such system is shown in Fig. 4.1. At its most basic, the setup consists of a parabolic mirror, a point light source and a filter (or knife edge). The light source and the knife edge were placed twice the focal length away from the parabolic mirror, and as close to each other physically possible. Due to the finite distance between the light source and the filter, the reflected beam does not take the same path back as the incident beam illustrated by Fig. 4.1. Two images would show up on the camera with a small offset. Shown in Fig. 4.2, as the distance between the object to the mirror increases, the image doubling becomes more severe. This image doubling was one of the main problems that needed to be solved to enable the mirror to be placed sufficiently far from the SPR test.

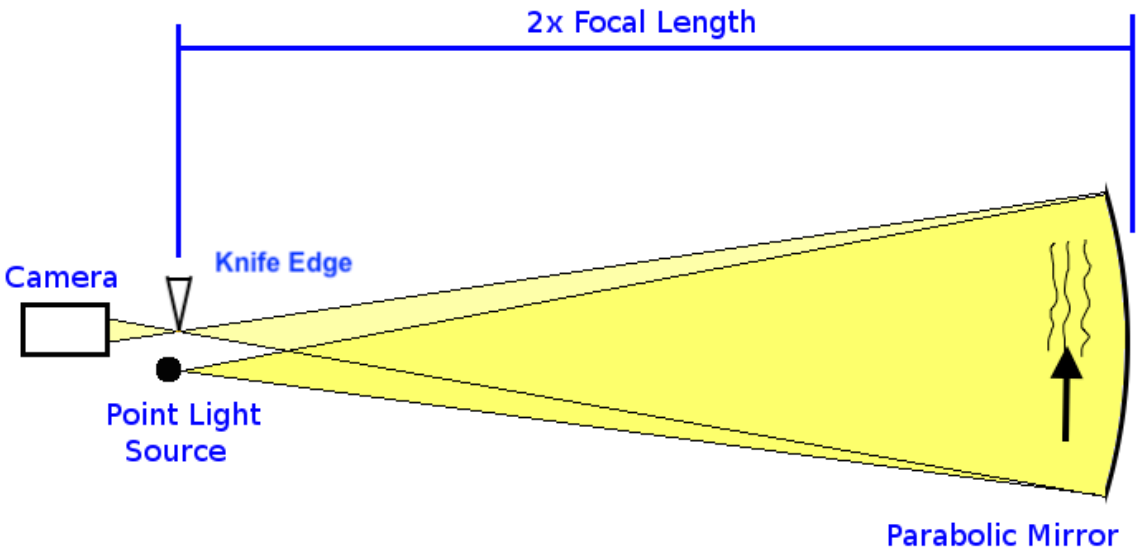

Figure 4.1: A basic single-mirror Schlieren system diagram: the incident beam does not take the same path as reflected beam

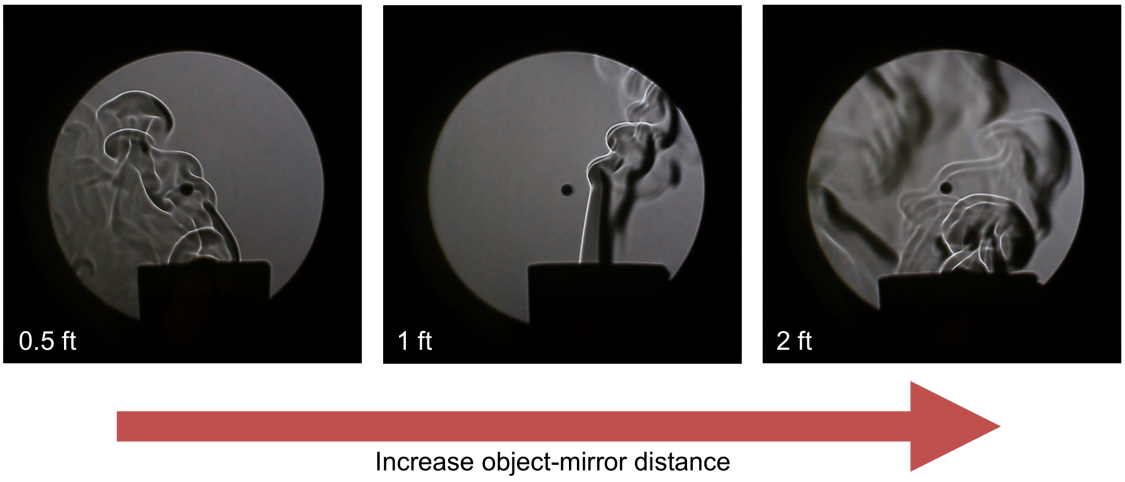

Figure 4.2: The image doubling effect on a single-mirror, coincident schlieren system: as the object to mirror distance increases, the image doubling becomes more severe

4.1.1 Optical Theory

A schlieren system is sensitive to the first spatial derivative of the refractive index: $\partial n/\partial y$. The relationship between refractive index, n, and a gas medium density, ρ, is described in the Eq. 4.1. Where k is Gladstone-Dale coefficient [13]. A shadow can be created by a non-constant second derivative of a density field which would show up on a shadowgraph set up, as illustrated in Fig. 4.3. The knife edge in a schlieren system enables the detection of a non-constant first derivative of a density field.

$$n - 1 = k\rho \tag{4.1}$$

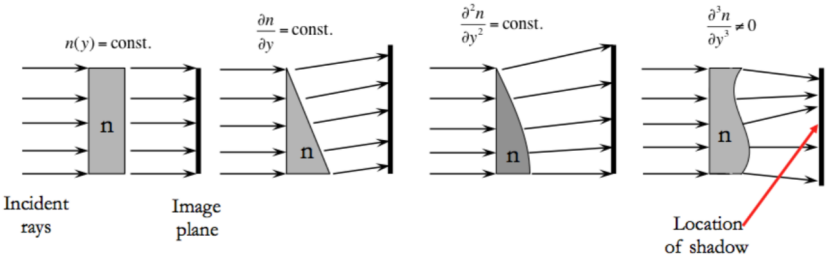

Figure 4.3: Schematic of light rays refracted by density fields with constant density and its first, second, and third derivative constant

Fig. 4.4 depicts the plane of the knife edge. The light source has a size of b $\times$ h. The uncut portion of the undisturbed light source has a height of a. The density gradient causes a weak displaced image to shift Δa distance in the y-direction. The amount of Δa is dependent on the schlieren system focal length and density gradient of the observing medium.

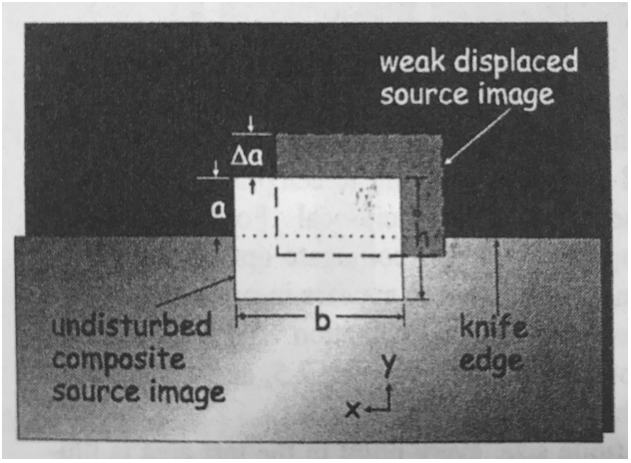

Figure 4.4: Diagram of the knife-edge plane [13]

Eq. 4.2 demonstrates that the amount that the image is shifted proportional to refraction angle ϵ_y.

$$\Delta a = f\epsilon_y \tag{4.2}$$

Contrast of a schlieren image is the ratio between differential illuminance at an image point, which is proportional to Δa, and general background illuminance, which is proportional to a. Eq. 4.3 demonstrates that the amount of knife edge cut-off incresases the constrast by decreasing the length of a.

$$C = \frac{f\epsilon_y}{a} \tag{4.3}$$

The sensitivity of any instrument is an influence coefficient, i.e. d(output)/d(input) [13]. The sensitivity of a schlieren system can be called contrast sensitivity, shown in Eq. 4.4, defined as the rate of change of image with respect to refraction angle.

$$S = \frac{dC}{d\epsilon} = \frac{f}{a} \tag{4.4}$$

The optical theory applies equally to all versions of the set up described in the following subsections.

4.1.2 Optical Improvements

The schematic of Tan (2018) schlieren system is shown in Fig. 4.5. In order to minimize the image doubling illustrated in Fig. 4.2, the mirror was placed as close to the test section as possible. Following the light beam path, the LED light is focused by the condenser lens onto the aperture, making the aperture an effective point source of light. Passing through the aperture, the light is focused at the knife edge after passing through the test section, reflected by the concave mirror and a small flat mirror (necessary because the camera could not be placed very closely to the aperture). The image doubling was barely visible as a result. However, setting the concave mirror less than two inches away from the Mach 2 Ludwieg tube freestream flow caused the mirror to shake during each test run. The background light intensity of each frame was not constant due to the mirror shake, as shown in Fig. 4.6. The usable number of frames were greatly reduced and challenges with interpretation were introduced .

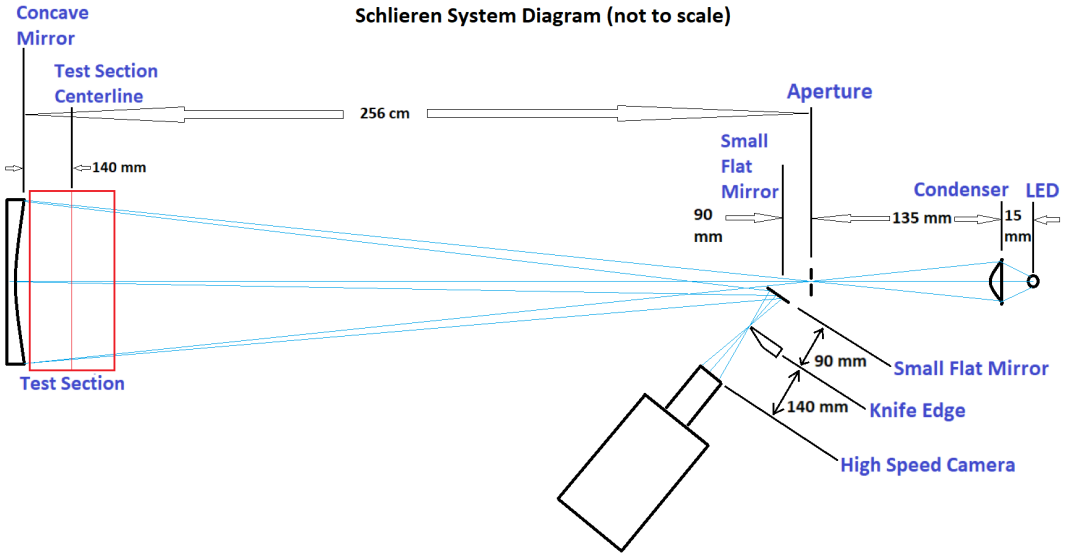

Figure 4.5: Tan (2018) schlieren system setup: the concave mirror was placed as close as possible to test section to reduce the image doubling

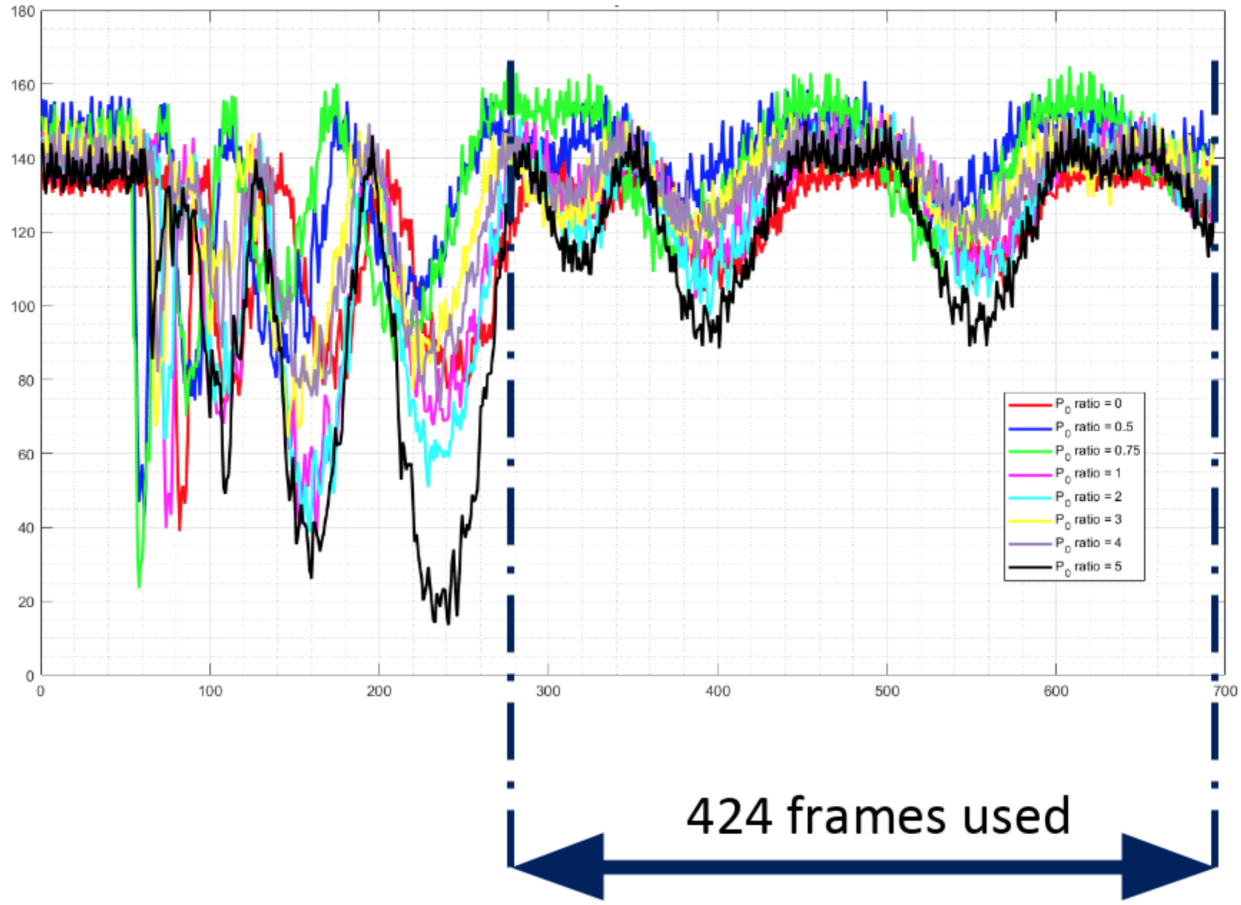

Figure 4.6: The average frame intensity of all test cases for Tan (2018) across all frames

A 50:50 beam splitter was introduced in the final version to replace the small plane mirror as shown in Fig.4.7. The incident beam takes the same path as the reflected beam. The image doubling is no longer dependent on the distance between the test section to the concave mirror. As a result, the mirror was moved far enough from the test section so that the mirror could not be disturbed by the impulse from the Ludwieg tube. The final setup of the schlieren system used in this thesis, as constructed in the lab, is shown in Fig.4.8. The green LED is a part of the pulsed LED light source system. The deisgn and construction of this system is addressed is addressed in the next section.

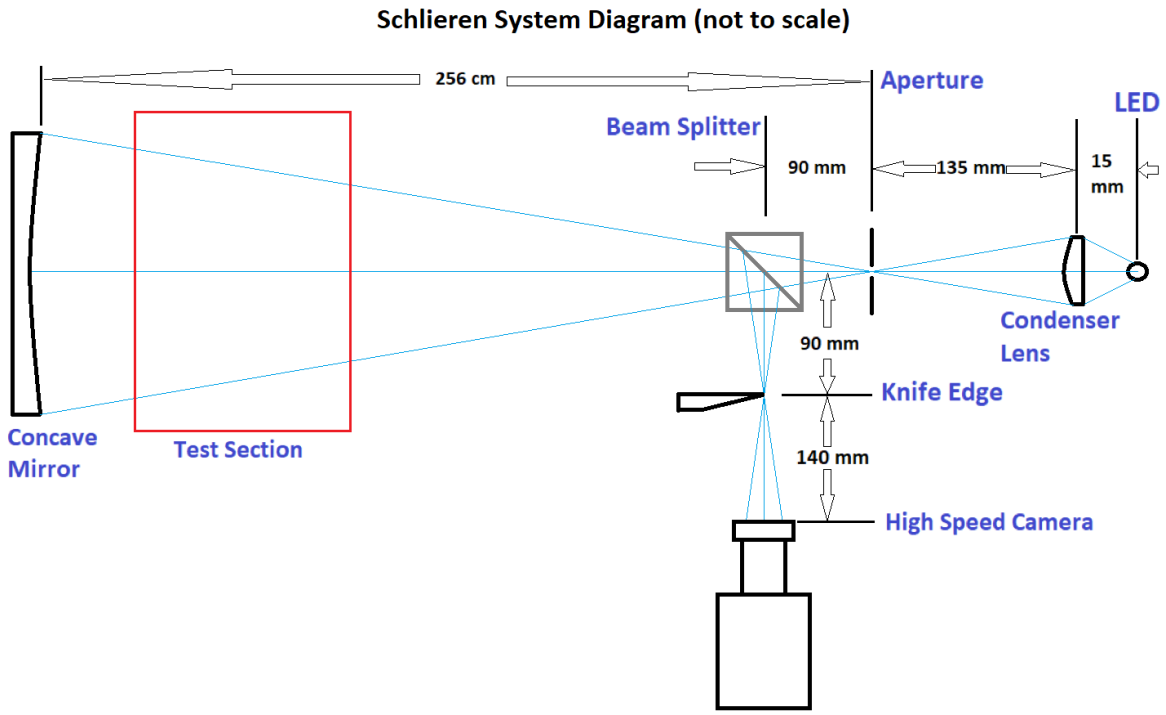

Figure 4.7: Version 4 schematic: incident beam and reflected beam were merged co-linear by a beam splitter

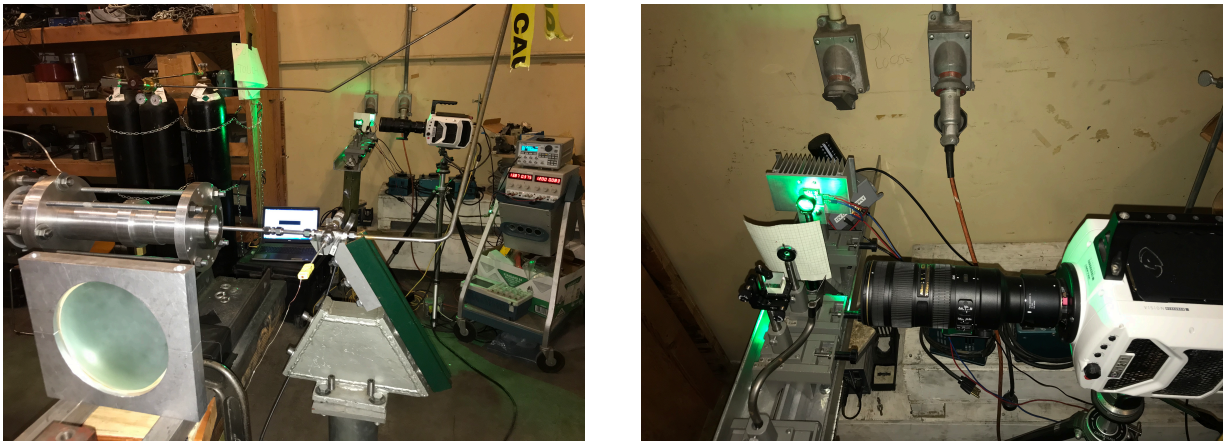

Figure 4.8: Version 4 set up: the entire length of the schlieren system visible on the left picture, optical components near the high-speed camera on the right picture

4.2 Overdriven LED Light Source Development

A light source with high intensity and short pulse was required fto freez the flow structures in time. In the SRP experiment, an order of 1 μs exposure time was needed to freeze flow detail in each frame. An LED pulsed circuit was created based on the design of Lincoln (2015) [14]. Fig. 4.9 shows the circuit diagram of the pulsed LED. The capacitor, C_{SUPPLY}, is charged by V_{SUPPLY}, and the MOSFET driver, U_1 is powered by V_{GATE}. When a trigger is detected by the MOSFET driver, the MOSFET transistor, M_1, acts as a closed switch. The capacitor is drained through the LED. Triggered by a function generator, LED pulse frequency was synchronized with the high-speed camera frame rate. The exposure time was determined by the LED pulse width. The circuit was first assembled on a breadboard and tested. A printed circuit board (PCB) was designed and manufactured after the breadboard prototype was verified to be functional.

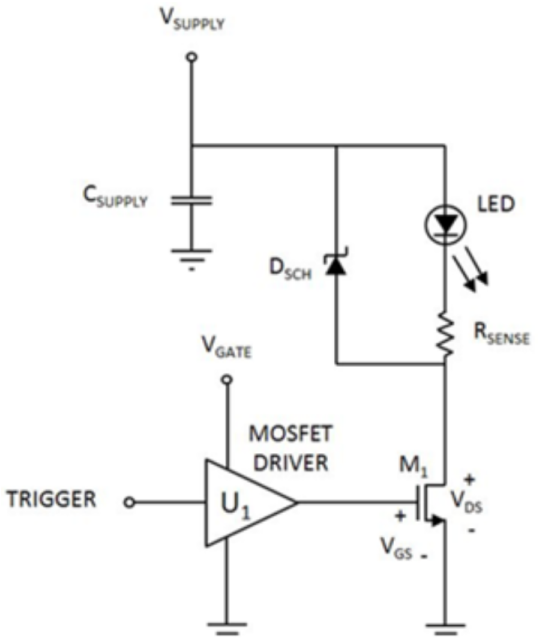

Figure 4.9: Lincoln (2016) [14] pulsed LED circuit design

4.2.1 Breadboard Prototype Assembly

The pulsed LED circuit was first assembled on a breadboard. Signals of different components were monitored to verify the functionality of the circuit design. The LED light was converted to an electrical signal by a photodiode, so the intensity of the LED could be monitored by an oscilloscope. A Sorsen XPL 30-2T triple DC power supply was used to power the capacitor and the MOSFET driver separately. V_{GATE} was kept at 12V. Variation of V_{SUPPLY} adjusted the pulse current during steady operation, which was measured through the voltage drop, R_{SENSE}. A function generator was used to trigger the circuit. A Tektronix TDS 2024B four-channel oscilloscope was used to monitor the trigger signal from the function generator, the signal output of the MOSFET driver, the voltage drop, R_{SENSE}, and the photodiode output that corresponds to the LED brightness.

Time traces of trigger signal, MOSFET driver output, and LED response signal from the photodiode, from CH1 to CH3 respectively are shown in Fig. 4.10 and Fig. 4.11. Noise from the breadboard was observed after the falling edge of the MOSFET driver output. In Fig.4.10, each LED pulse required another 4 μs for the LED to turn off after the trigger pulse dropping back to zero volts. The breadboard prototype verified that the circuit design by Lincoln (2016) was functional, but left room for improvement. The improvements include, but not limited to: decrease the signal oscillations, decrease the signal noise, and increase the LED response speed. A PCB with wide traces and better noise shielding was needed to further enhance the cleanness and responsiveness of the signals by optimizing the connections between components.

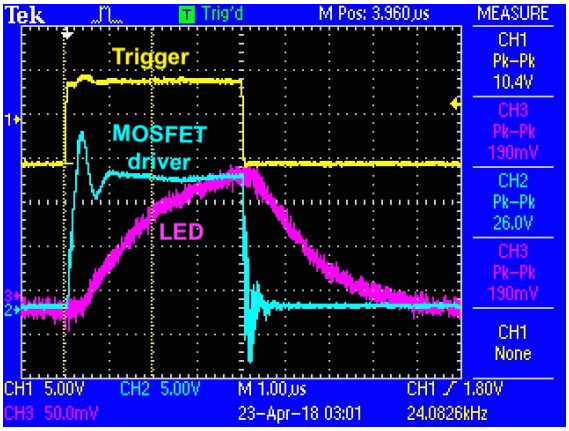

Figure 4.10: LED response to 4 μs square wave, breadboard prototype

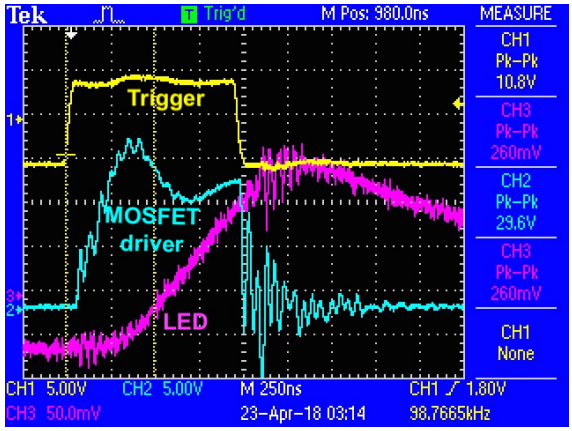

Figure 4.11: LED response to 1 μs square wave, breadboard prototype

4.2.2 PCB Design, Manufacturing and Testing

A printed circuit board (PCB) was designed to reduce response time and smooth the LED signal. Thick traces were mapped on the PCB, so the internal resistance of the circuit was minimized. A common ground plane on either side of the PCB was shared among U_1, M_1, and C_{SUPPLY}. Two terminals parallel to the MOSFET driver power supply were added to power two computer cooling fans. Components were soldered on the PCB and enclosed in a box as the LED driver unit. Power supplies, trigger, and the LED terminals were externally connected to the unit.

The circuit performance of the pulsed LED PCB was verified using an oscilloscope to capture the signals of various components. The experimental setup of the verification is shown in Fig. 4.12. CH1 corresponded to the trigger signal, CH3 presented the LED response, and CH2 was used to probe both the MOSFET driver output and voltage drop, R_{SENSE}, shown in Fig. 4.13 and Fig. 4.14 respectively. Compare to the previous result in Fig. 4.10, the MOSFET driver output signal exhibited less ringing after the falling edge of the trigger signal. In Fig. 4.14, the voltage drop across R_{SENSE} was measured to be 2V (CH2), which corresponds to 400 A LED current, over 20 times the rated current (18 A). The current was

calculated by dividing voltage drop (2V) by resistance of R_{SENSE} (0.005 Ω). An approximate 125 ns delay between the trigger and the LED start current was observed, which was caused by the MOSFET driver latency[17].

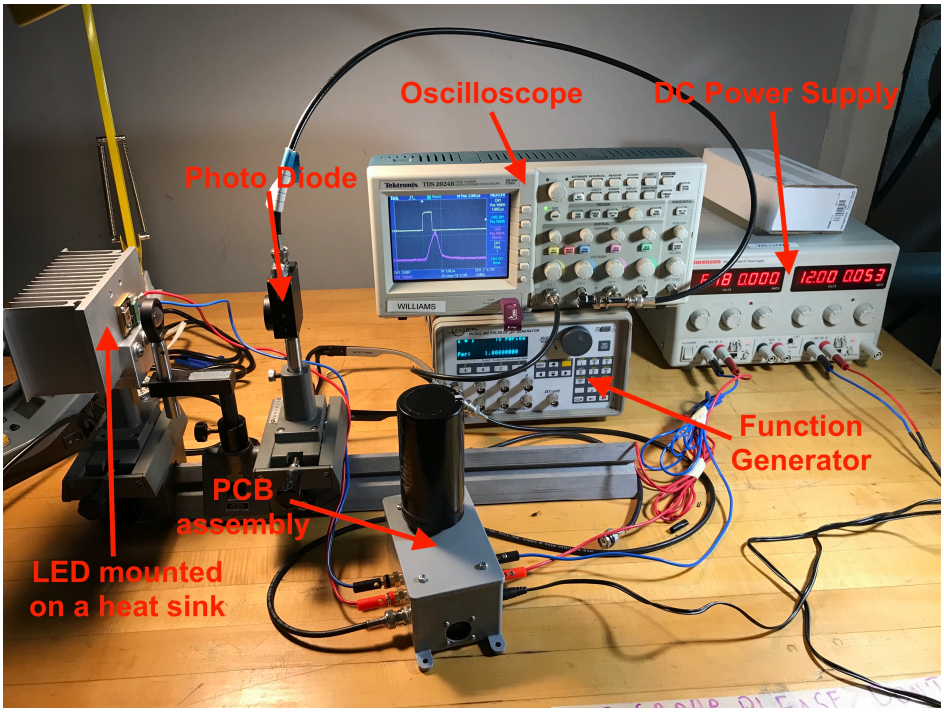

Figure 4.12: The experimental setup of the PCB verification test with critical equipment labeled

In Fig. 4.15 and Fig. 4.16, 1 μs light pulse was captured. The pulse width of the LED was similar to the trigger pulse width. Comparing to Fig. 4.11, the breadboard result, the LED emitted shorter and cleaner pulses. The circuit response was significantly improved by PCB implementation. Comparing Fig. 4.16 and Fig. 4.11, less noise was observed on the LED light signal. The input trigger from the function generator was less disturbed by the noise from the circuit. Furthermore, the time required for the LED to dim was significantly decreased.

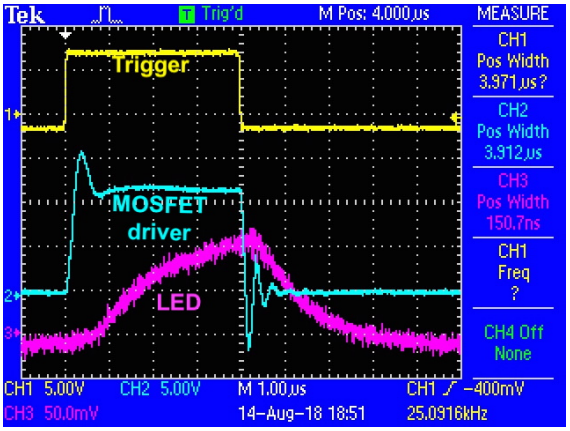

Figure 4.13: MOSFET on CH2

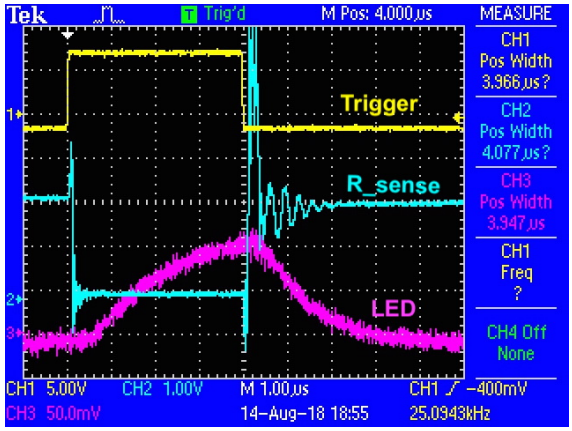

Figure 4.14: R_{sense} voltage drop on CH2

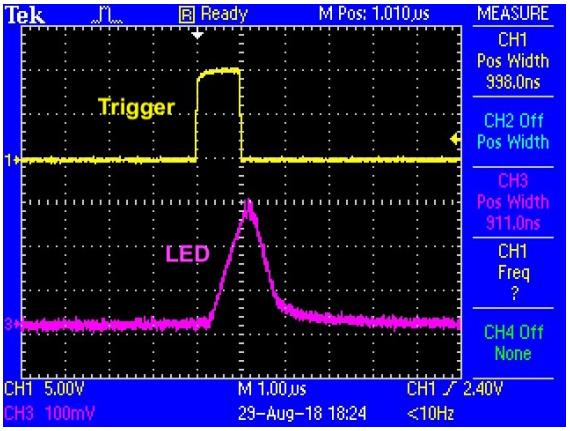

Figure 4.15: 1 μs trigger

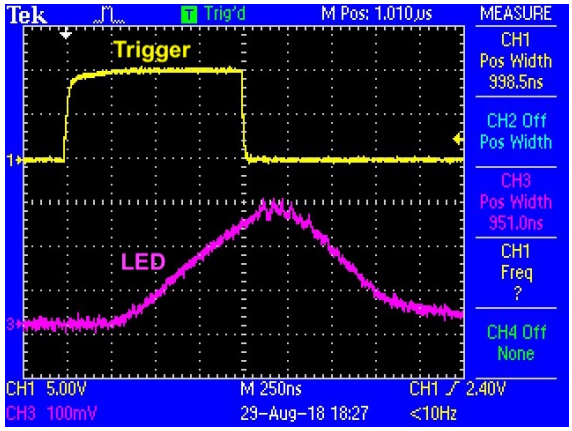

Figure 4.16: 1 μs trigger, magnified

The LED light source was integrated within the schlieren system. The setup was shown in Fig. 4.8. The difference in image quality before and after the pulsed LED implementation is shown in Fig. 4.17. For Tan (2018) study, schlieren data was acquired at 37,000 fps and with 8 μs exposure time using a continuous light source. Both pictures of Fig. 4.17 are snapshots of a supersonic retropropulsion flowfield under identical flow conditions. For the current design, the pulse width of the LED dictated the exposure time of each frame. On the right picture of Fig. 4.17, taken at 76,000 fps, 1 μs LED pulse width, flowfield structures

are sharper as they are frozen in in time compared to Tan (2018) result. The high intensity of the pulsed LED also helped increase the brightness of the overall image.

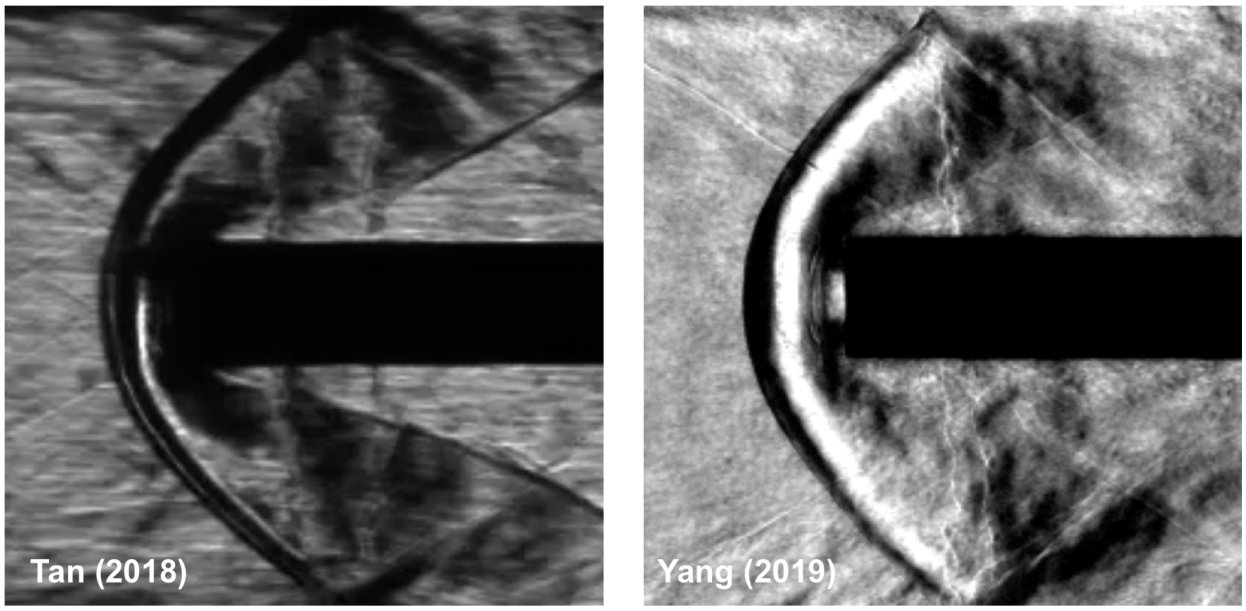

Figure 4.17: The comparison between Tan (2018)

In the experiment, the 1 μs width LED pulse was pulsed at 76,000 Hz. The duty cycle used for the LED was 7.6 %. Running on 20 times the rated current, it is suggested not to exceed such duty cycle to prevent damage to the LED.

4.3 Image Analysis

4.3.1 Mean and RMS

The mean and RMS images of each high-speed schlieren video were computed to identify the structure and dynamics of the SRP flows. Eq. 4.5 calculates the mean image of a video consisting n number of frames with i × j pixel image size.

$$\bar{x}_{ij} = \frac{1}{n}(\sum_{k=1}^{n} x_{ijk}) = \frac{x_{ij1} + x_{ij2} + ... + x_{ijn}}{n} \tag{4.5}$$

Eq. 4.6 calculates the RMS image of a video that consists n number of frames with i × j pixel image size. An RMS image presents motion occurred in a video, so the more dynamic regions could be highlighted.

$$x_{ij,RMS} = \sqrt{\frac{1}{n}\sum_{k=1}^{n}(x_{ijk} - \bar{x}_{ij})^2} = \sqrt{\frac{(x_{ij1} - \bar{x}_{ij})^2 + (x_{ij2} - \bar{x}_{ij})^2 + ... + (x_{ijn} - \bar{x}_{ij})^2}{n}} \quad (4.6)$$

4.3.2 Nozzle Stabilization

Located at the center of the Ludwieg tube flow, the retro nozzle was pushed up and down due to the aerodynamic forces on the retro nozzle assembly. A stabilization method was developed by Ho (2019) [18]. K-mean segmentation was applied to the schlieren raw .cine data, binarizing each frame into black and white, so that white represents the nozzle. The center of the nozzle tip was located by finding the white pixels in X and Y directions of each frame. Once the nozzle was tracked, a polynomial fit was applied to model the nozzle position and this position was used to crop the video such that the center of the nozzle tip always stayed at the center of each frame.

Chapter 5

RESULTS AND DISCUSSION

The tri-nozzle was tested at three stagnation pressures and compared with four single-jet nozzles shown in Fig. 5.1. The freestream condition was Mach 2, with a static pressure of sea level atmospheric condition. The stagnation pressure of the freestream was calculated using isentropic relations. The pressures at which tests were conducted for all six nozzles are shown in Table 5.1. For all test cases, high-speed schlieren video was acquired with a resolution of 384×288 pixels at 76,000 fps and 1.75 μs exposure time. Due to the aerodynamic force acting upon the retro nozzle by the freestream, the nozzle tip was observed to move slightly in each video. This motion was small but large enough to distort the calculation of mean and RMS flowfields. The nozzle tip was tracked and stabilized using a method developed by Ho (2019) [18]. The available frames for each dataset, after stabilization, are shown in Table 5.2.

Table 5.1: Experimental test conditions for varying $P_{0,ratio}$

$P_{0j}/P_{0\infty}$	P_{0j} [psi]
0.5	57.5
1.0	115
5.0	575

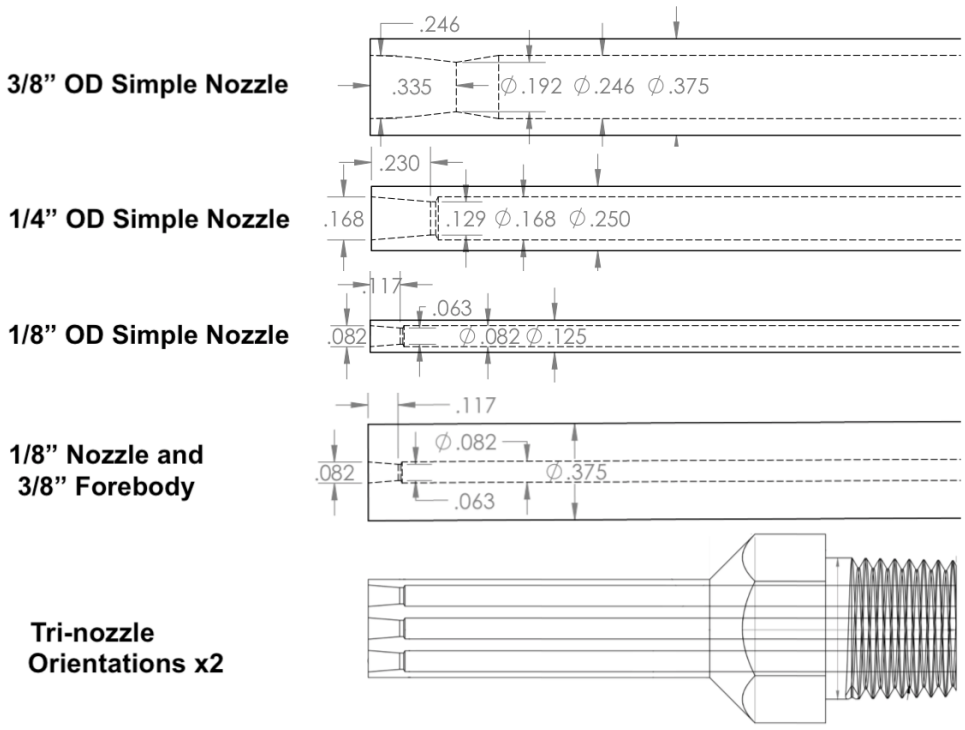

Figure 5.1: All nozzle configurations

Table 5.2: Available frames for each test case after nozzle stabilization (FB stands for forebody)

Retro Nozzle Type	$P_{0j}/P_{0\infty} = 0.5$	$P_{0j}/P_{0\infty} = 1.0$	$P_{0j}/P_{0\infty} = 5.0$
3/8" OD	943	439	349
1/4" OD	681	811	664
1/8" OD	505	516	505
1/8" OD + 3/8" FB	786	833	860
3/8" Tri-Nozzle, Vertical	993	1024	1065
3/8" Tri-Nozzle, Horizontal	1048	1013	1011

5.1 Examination of Flowfield with Scale of Simple Nozzle

The 3/8" OD simple nozzle was studied by Tan (2018) [4]. A subset of three pressures from her dataset was repeated for this study using the improved schlieren system and with the inclusion of image stabilization at $P_{0,ratio} = 0.5$, 1, and 5. Two other geometrically similar simple nozzles of outer diameters of 1/4" and 1/8" were tested under the same P_0 ratios. This study was conducted to determine if the scale of the 3/8" (relative to the 2" diameter freestream) had a significant influence on SRP flowfield patterns and observed periodic unsteadiness at $P_{0,ratio} = 1$.

Even though the nozzle tip was stabilized, the angle of attack of the nozzle changes very slightly on a time scale of hundreds of frames. In each case, only 200 continuous frames were chosen for mean and RMS image construction. The chosen number of frames have a time scale less than 1/4 of the nozzle motion period while also being long relative to other flow features.

In Fig. 5.2, the mean images of the simple nozzles are presented for the three test pressures. Flowfield features appear to be highly similar across difference nozzle sizes under the same test condition, which suggests that the scale of the 3/8" nozzle, relative to the freestream flow is having little effect on flowfield topology. It is also seen that as the value of $P_{0j}/P_{0\infty}$ decreases, the shock standoff distance and the shock radius of curvature decreases. At P_0 ratio = 5, the shock fronts are located farthest to the nozzle exit, and sharp jet structures and shock boundaries are visible. At unity pressure ratio, the shock boundaries are more diffuse compared to other pressure ratio cases, indicating more motion. Both high and low pressure ratios have sharp shock boundaries, suggesting little motion.

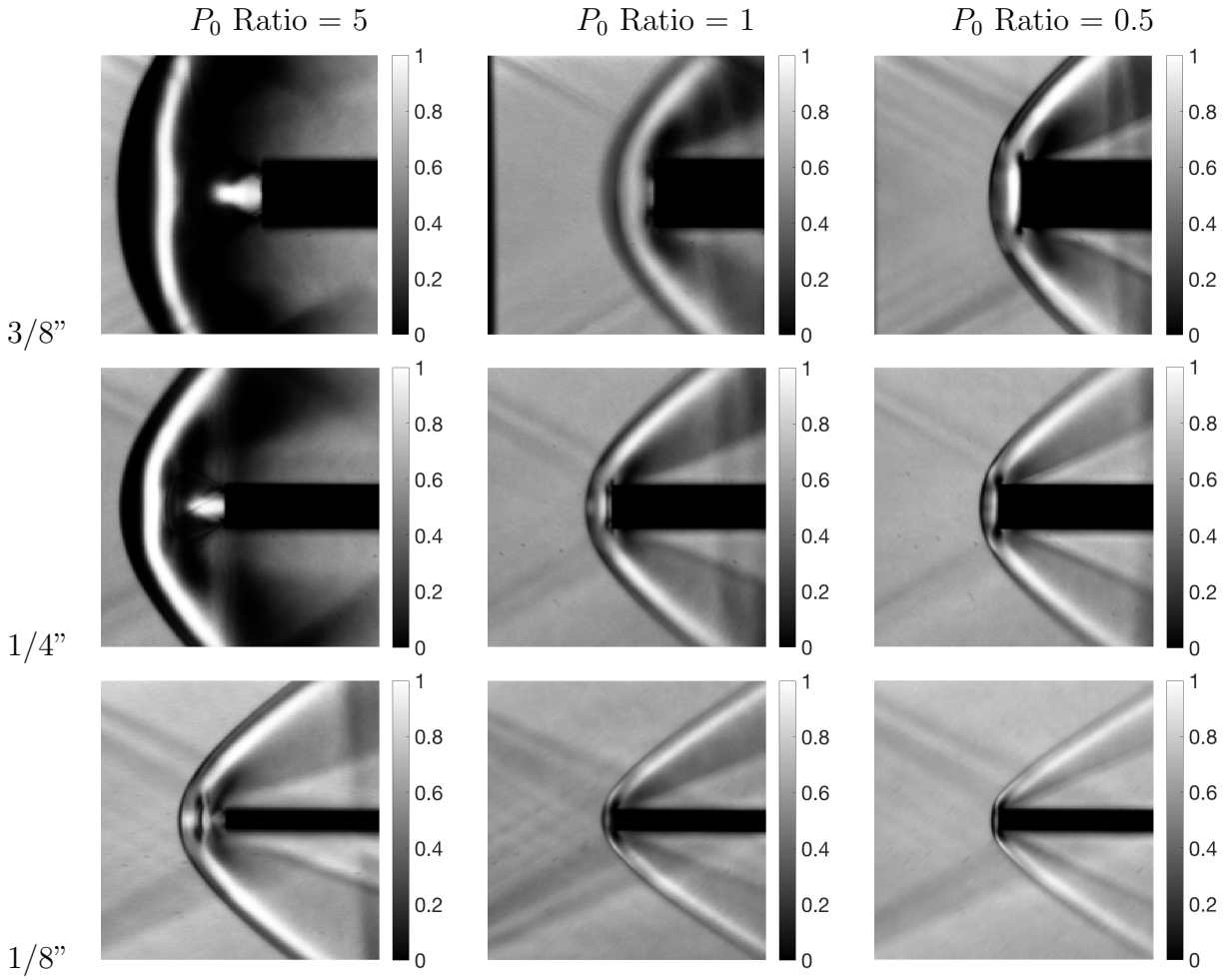

Figure 5.2: The mean image of SRP flowfield for all simple nozzles at all test conditions

Simple nozzle RMS images are presented in Fig. 5.3. Flowfields for all three nozzle sizes once again have highly similar topology under the same test conditions, further verifying the 3/8” OD nozzle results’ accuracy. Some common flowfield features of many of the test cases are highlighted in Fig. 5.4, which depicts the 3/8” nozzle with a pressure ratio of 0.5. A ”triple band” feature on the RMS images can be seen on all nozzle cases except the 3/8” nozzle with a unity pressure ratio due to the large extent of shock movement. Upon examination of the mean images, these bands occur on the boundaries of large intensity

variation. Schlieren images indicate the first derivative of the density. An abrupt change in density is introduced by a shock. Vertical bands behind the bow shock are the results of bow shock-to-supersonic freestream flow edge interaction which is more upstream for larger nozzles. An expansion region of higher RMS is also visible in many cases.

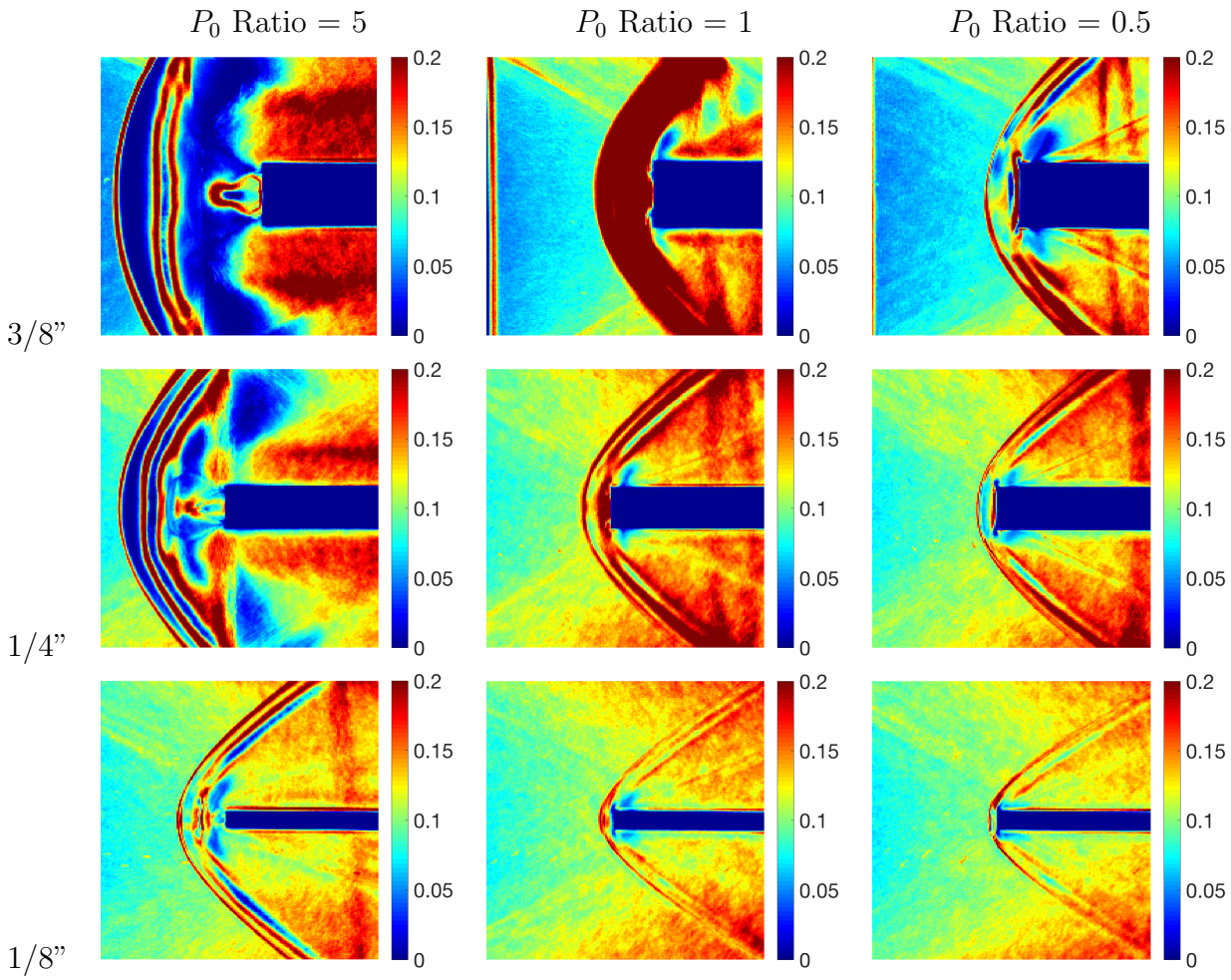

Figure 5.3: The RMS image of SRP flowfield for all simple nozzles at all test conditions

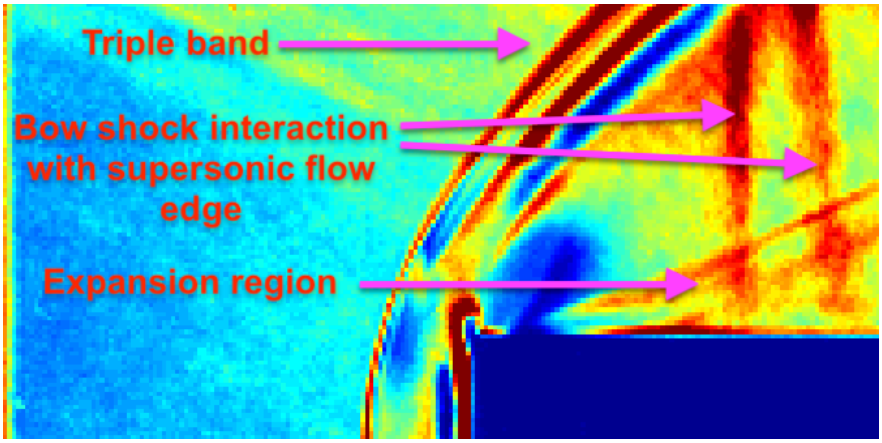

Figure 5.4: Common features seen on a SRP flowfield labeled on 3/8" OD simple nozzle, P_0 ratio = 0.5

For P_0 ratio = 5, and 0.5 flow structures in the vicinity of the nozzle exit appear to be highly similar and very stable across different nozzle sizes under the same conditions. RMS on the shock edges appears to be as thin as few pixels. For $P_0 = 5$, continuous triple band features are observed on the shock. At $P_0 = 0.5$, little differences in flowfield can be observed across different cases.

At unity P_0 ratio, large shock movements are seen in the front of the retro-nozzles. For the 3/8" OD nozzle, wide band of high RMS is visible along the bow shock curvature, highlighting the most pronounced shock movement, and this result corresponds to the result of Tan (2018) at unity P_0 ratio. Periodic oscillatory motion of the entire bow shock is observed. For 1/4" OD and 1/8" OD nozzles, the flowfield topology is similar. Oscillatory shock motion can be seen on these smaller nozzles also. Larger RMS can be observed directly in front of the nozzle tip compare to $P_{0,ratio} = 0.5$ cases. Regions containing more motions could still be indicated near the shock boundaries, but not as strong as the 3/8" nozzle. Smaller nozzle having thinner RMS bands is expected because the maximum movement of the shock is less (relative to the size of the pixels). The unsteadiness of the simple nozzles is compared to the tri-nozzle unsteadiness characteristics in the next section.

5.2 Tri-Nozzle Configuration

The tri-nozzle was tested at the same pressure ratios (0.5, 1, and 5) at two orientations (vertical and horizontal) so that potential directional asymmetry of the tri-nozzle flowfield can be examined. Similarly to the simple nozzle cases, 200 frames were used to construct the mean and RMS images. The tri-nozzle is compared with the 3/8" OD simple nozzle and the 1/8" OD simple nozzle having a 3/8" OD forebody sleeve installed. The nozzles are shown in Fig. 5.5. Flowfields at P_0 ratio = 5, P_0 ratio =1, and P_0 ratio = 0.5 are presented by Fig. 5.6, 5.7, and 5.8 respectively.

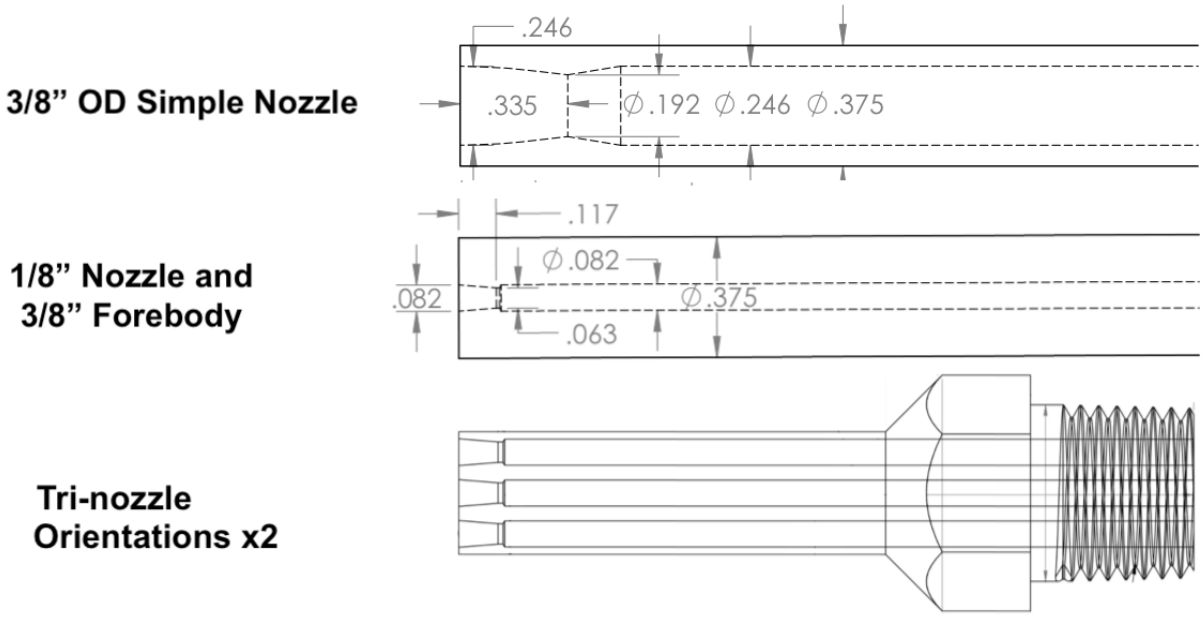

Figure 5.5: The nozzles used in the tri-nozzle study

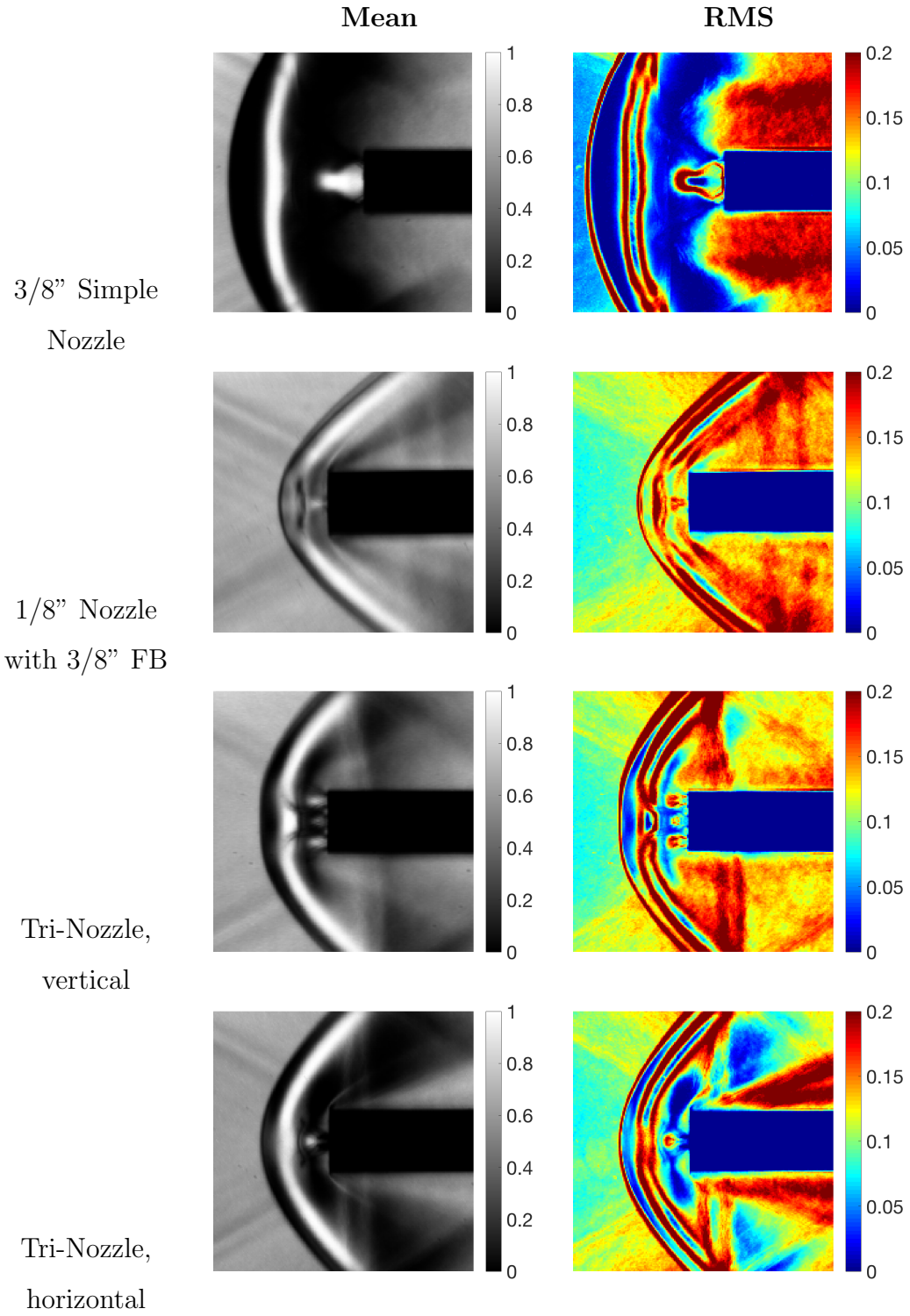

Figure 5.6: The (left) mean image and (right) image of SRP flowfield comparison at P_0 Ratio = 5

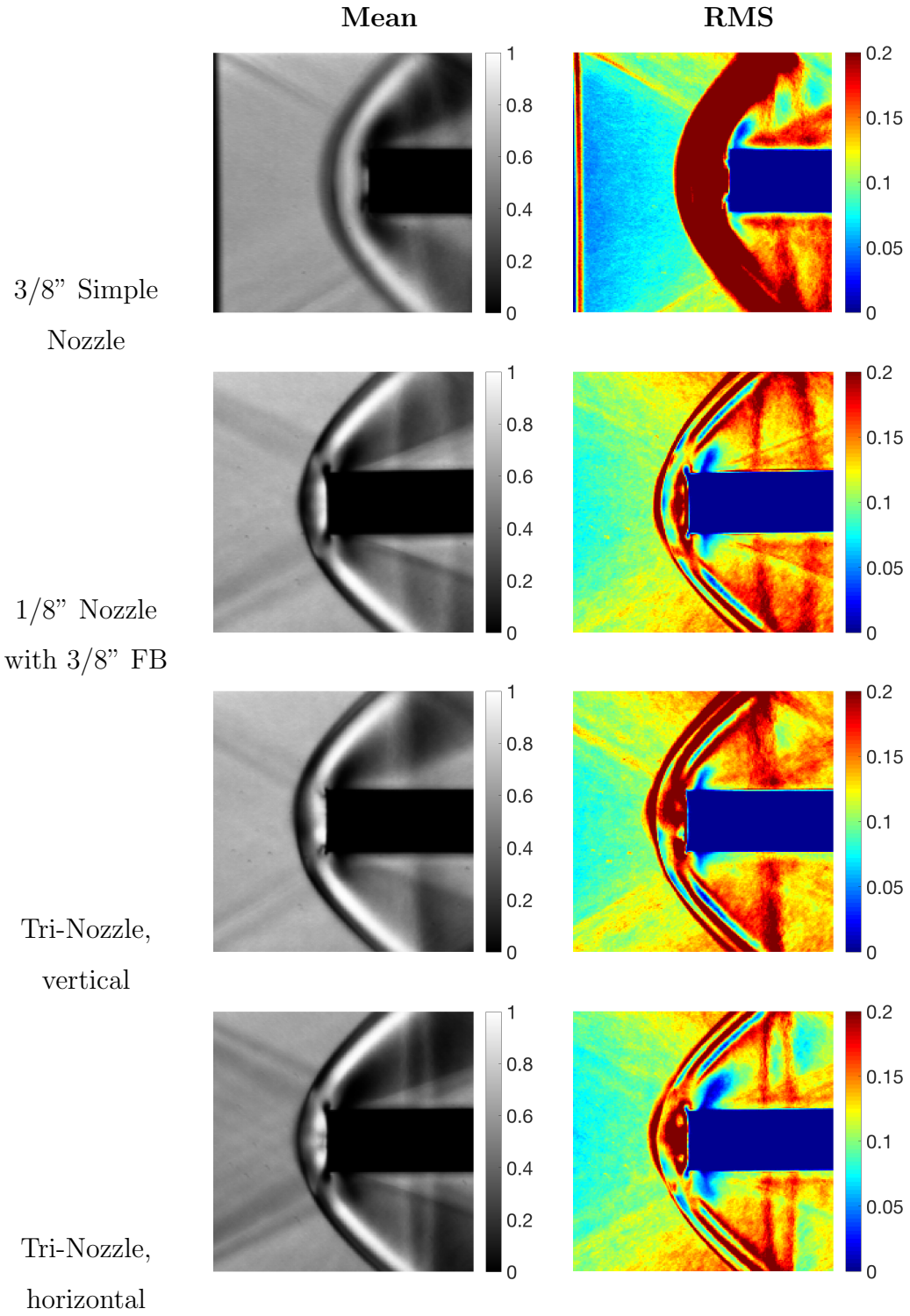

Figure 5.7: The (left) mean image and (right) image of SRP flowfield comparison at P_0 Ratio = 1

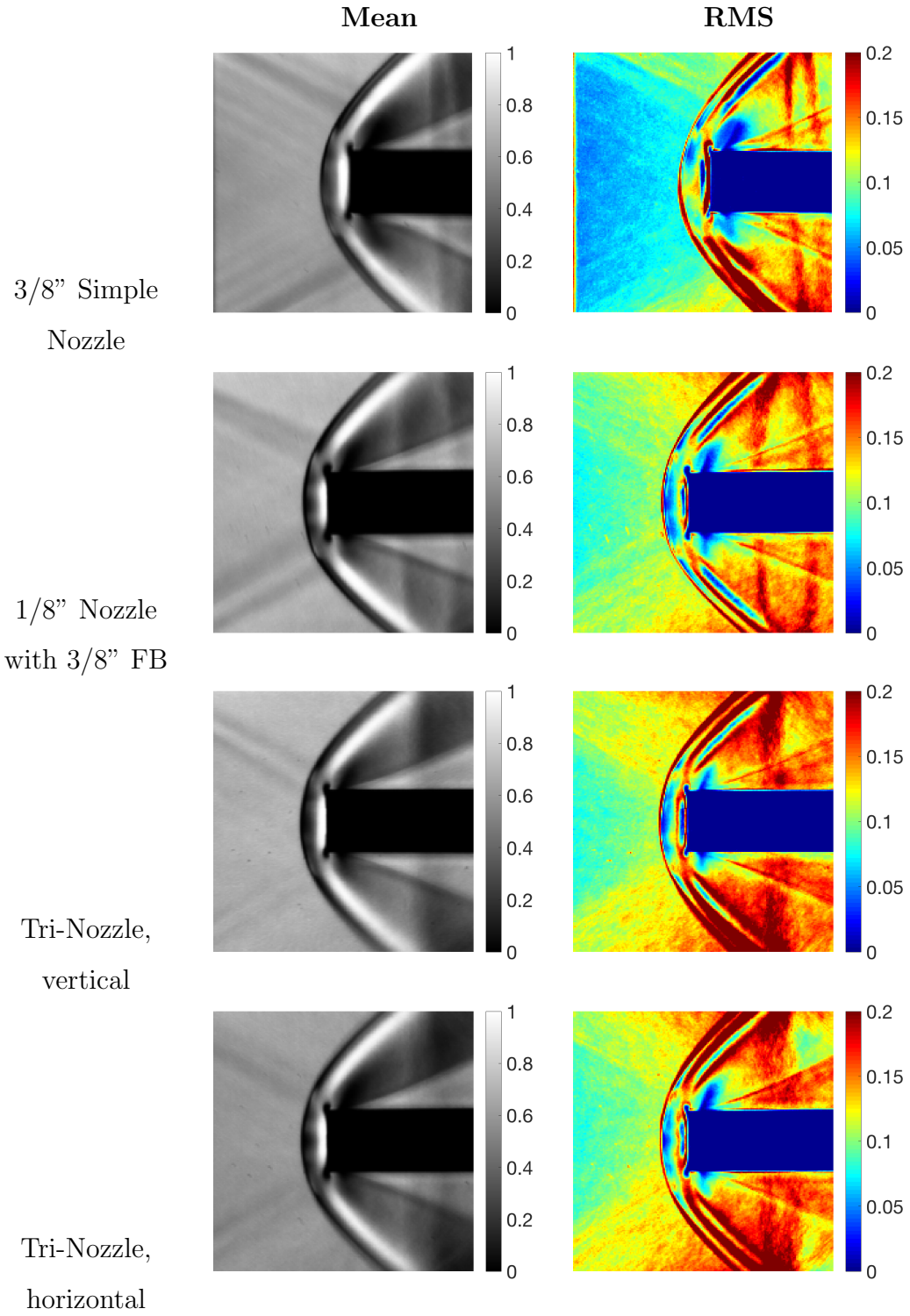

Figure 5.8: The (left) mean image and (right) image of SRP flowfield comparison at P_0 Ratio = 0.5

5.2.1 Flowfield Overview

Based on mean and RMS images, steady flowfields are observed for all nozzles at P_0 ratio = 5 and 0.5. For the cases of P_0 ratio = 0.5, shown in Fig. 5.8, mean and RMS images are very similar to one another. It is difficult to distinguish the types of nozzle based on the flowfield features. All cases have very stable bow shocks with sharp, clearly defined edges that are as thin as few pixels. Common flow features indicated by Fig. 5.4 can be seen in all nozzles with a pressure ratio of 1/2.

Steady flowfields for P_0 ratio = 5 have many unique features for different types of nozzles and nozzle orientations. In Fig. 5.6, the tri-nozzle mean and RMS flowfield images at P_0 ratio = 5 are compared with the 3/8" OD simple nozzle and the 1/8" OD simple nozzle with 3/8" forebody. The largest bowshock standoff distances appear at P_0 ratio = 5 cases. In the vertical orientation, three jets are visible. The stable jet structure is indicated by the clear, thin RMS band near the shock front, similar to the 3/8" OD simple nozzle. Larger bow shock radius of curvature is observed in the vertical orientation compare to horizontal orientation. Directly in front of the nozzle, the shock is almost flat, having a large portion normal to the freestream. At the center of the bow shock, the interaction of multiple jets with the bow shock causes a series of discontinuous RMS bands to appear as seen in Fig 5.9. A "double band" feature between the front of the bow shock and the jet can be observed for the 3/8" OD simple nozzle and tri-nozzle horizontal cases. On the tri-nozzle vertical case, the "double band" is cut off at the location where the band is intersecting the outboard jets. This region contains interaction among three jets. The center jet appears to be more steady than the two outboard jets. The boundary of the center jet experiences less velocity difference than the outboard jets.

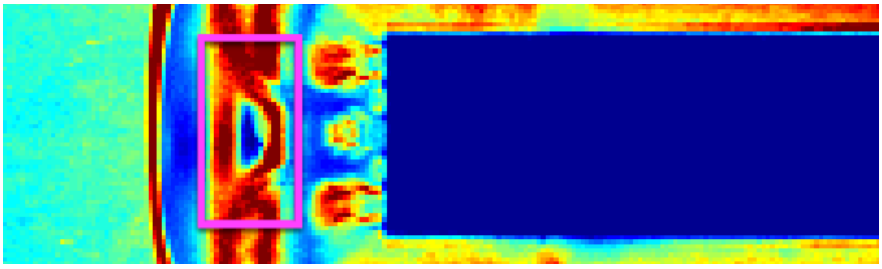

Figure 5.9: Discontinuous"double band" feature near jet-to-jet interaction region

In the horizontal orientation, the bow shock structure of the tri-nozzle is very similar to the 1/8" nozzle with 3/8" forebody case. The "double band" between the shock and jets appears to be continuous. The tri-nozzle bow shock has a smaller radius in the horizontal orientation and larger than the 1/8" nozzle with 3/8" forebody. At $P_{0,ratio} = 5$, directional asymmetry can be observed. It should be noted that for the tri-nozzle horizontal orientation, the expansion region downstream of the nozzle tip has a high RMS as shown in Fig 5.10. The hypothesis suggests that in the high RMS region, small eddies are shed from the nozzle tip more than any other cases.

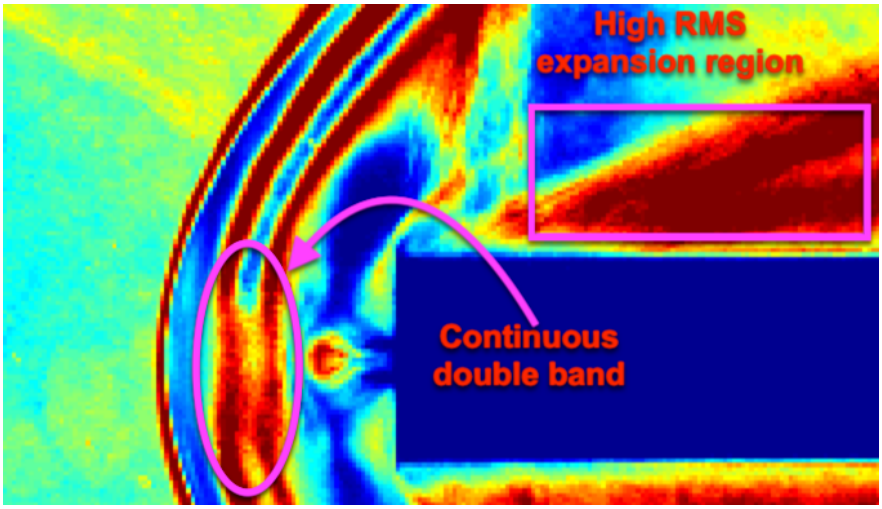

Figure 5.10: Large RMS downstream the highly visible expansion fan in the tri-nozzle horizontal orientation at P_0 ratio = 5

Unsteadiness of the bow shocks can be observed for all the unity pressure ratio cases. The characteristics of the unsteadiness are affected by the nozzle geometry. For all the simple nozzles, an unsteady flowfield is characterized by the entire bow shock oscillating forward and backward periodically without obvious geometrical change. The oscillation of the entire shock front is seen most prominently for the 3/8" OD simple nozzle: a wide band of high RMS along the bow shock curvature indicates uniform movements of the bow shock. For the other cases, oscillations do not occur on the shock uniformly. Bow shock penetration can be observed on the 1/8" nozzle with 3/8" forebody and the tri-nozzle. The tri-nozzle flowfield at unity pressure is similar for both orientations. Some common features are shared among these cases, and they are presented in Fig. 5.11. Directly in front of the nozzle tip, two regions of high RMS can be observed: one directly attached to the nozzle, and the other on the shock front. The shock front has a minimum thickness of RMS at inflection points. All these common features are indicators of more motions concentrating directly in front of the nozzle. The more irregular RMS regions directly in front of the vertical tri-nozzle case could indicate that instabilities in the three jets at unity pressure ratio interacting with each other creating more instabilities in the overall flowfield. The unsteadiness characteristics will be further discussing in the next section.

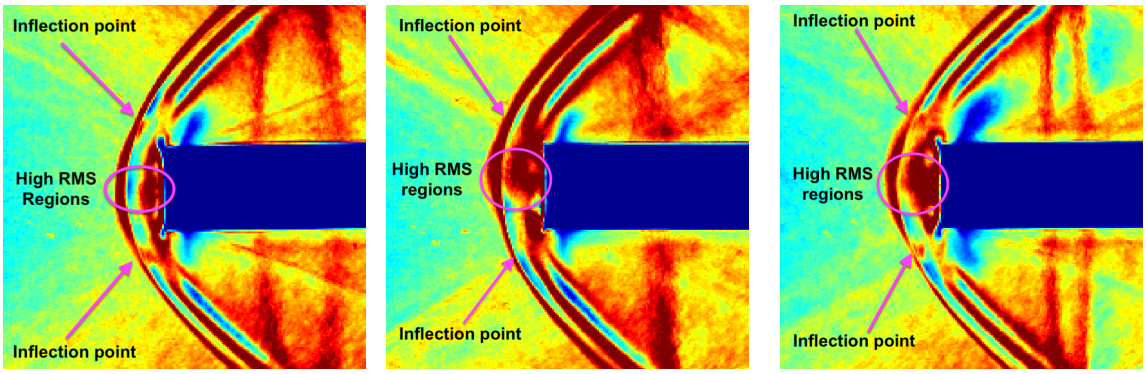

Figure 5.11: Common features of the flowfields are highlighted. Left picture: 1/8" simple nozzle with 3/8" forebody. Middle picture: tri-nozzle vertical orientation. Right picture: tri-nozzle horizontal orientation.

5.2.2 Bow Shock Standoff Distance

Bow shock standoff distance increases with jet pressure. For every test cases, the distance is examined. The average bow shock standoff distance is determined for each case using the mean image. The variation in shock standoff distance with jet pressure, normalized by the body diameter, is shown in Fig. 5.12. Error bars represent the maximum observed movement of the shock. All lengths are normalized by the nozzle body diameter, D_B. Table. 5.3 presents the nozzle body diameter for each nozzle type.

A comparison of jet standoff distance relative to jet hydraulic diameters is shown in Appendix B, however, correspondence between cases was not improved.

At $P_{0,ratio} = 0.5$, the steady nature of the flowfields are indicated by small error bars. All nozzles have similar normalized bow shock standoff distances within uncertainty. The nozzle exterior geometry is the more dominant factor that affects the standoff distance.

At P_0 ratio $= 1$, the standoff distance increase compare to 1/8" nozzle with 3/8" forebody and the tri-nozzle have much increase compared to the simple nozzle cases. The unsteady flowfield is indicated by tall error bars. The tri-nozzle and the 1/8" nozzle with 3/8" forebody have error bars overlapping their $P_{0,ratio} = 0.5$ cases.

The highest jet mass flow rate occurs at $P_{0,ratio} = 5$. The jet has the most dominant influence on the bow shock standoff distances. The simple nozzles have the same normalized bow shock standoff distance within uncertainty. Small error bars are observed in all cases, suggesting stable flowfields. The least amount of standoff distance increase is observed on 1/8"nozzle with 3/8" forebody. It has the least standoff distance among all six cases as expected by the smaller mass flux of the jet. The tri-nozzle has a standoff distance greater than the 1/8" nozzle with 3/8" forebody. The difference in bow shock standoff distance at P_0 ratio $= 5$ directly reflects the jet mass flow rate for each nozzle type.

Table 5.3: Nozzle body diameter for every nozzle used in the experiment

	3/8" OD simple	1/4"OD simple	1/8" OD simple	1/8" jet + 3/8" FB	Tri-nozzle
Body Diameter, D_B	0.375"	0.250"	0.125"	0.375"	0.375"

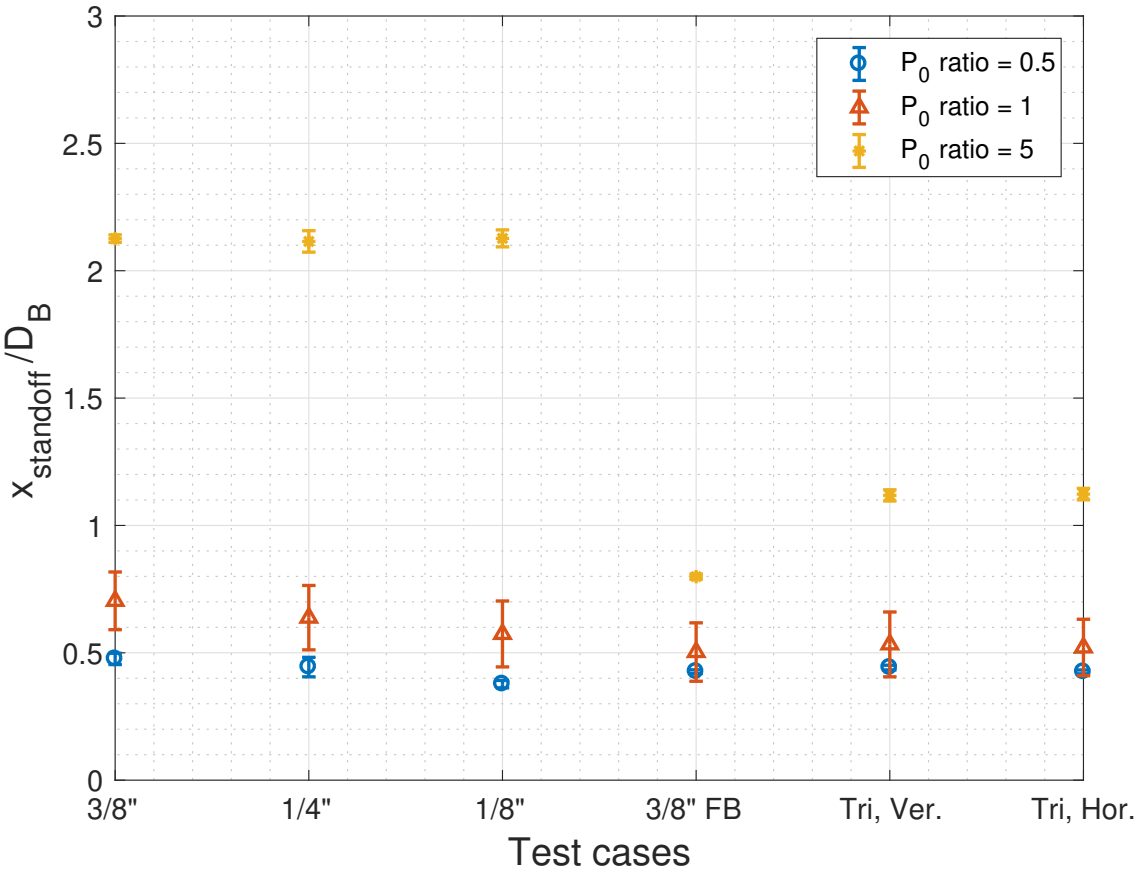

Figure 5.12: Bow shock standoff distance normalized by jet hydraulic diameter

5.2.3 Flowfield Unsteadiness

The unsteadiness of the bow shock for the different cases is qualitatively compared in Fig. 5.13. Two snapshots of each unsteady cases were taken. The forward-most and the backward-most positions of the bow shock are marked to show the magnitude of the motion. All simple nozzles have uniform oscillations along the entire shock curvature, and the shock motions of the 3/8" OD simple nozzle are similar to Fig. 1.4 shown by Tan (2018).

For the 1/8" nozzle with 3/8" forebody and the tri-nozzle cases, the manner of unsteadiness is similar. Erratic shock penetration and rippling is observed in both cases and both orientations of the tri-nozzle. A bulge at the center of the bow shock would momentarily appear, disrupting the smooth curvature of the shock front. Based on visual inspections, the rippling of the shock is occurred randomly, without identifiable, single-frequency oscillatory motions possessed by the simple nozzles. Rippled shock front can be observed. The percentage of this bow shock rippling throughout each test cases is estimated by visually examining each frame of the video. Any frame having a bulge in the front of the nozzle tip that introduces a disruption to the smooth shock curvature is counted as a distorted shock. The fraction of bow shock distortion time is recorded in Table. 5.4. A single jet on the forebody has approximately more than twice the bow shock distortion time than the tri-nozzle. As the nozzle-to-forebody base area ratio increases, the fraction of bow shock distortion decreases. The two orientations of the tri-nozzle were expected to produce the same fraction. However, sampling error between each test run introduced uncertainty.

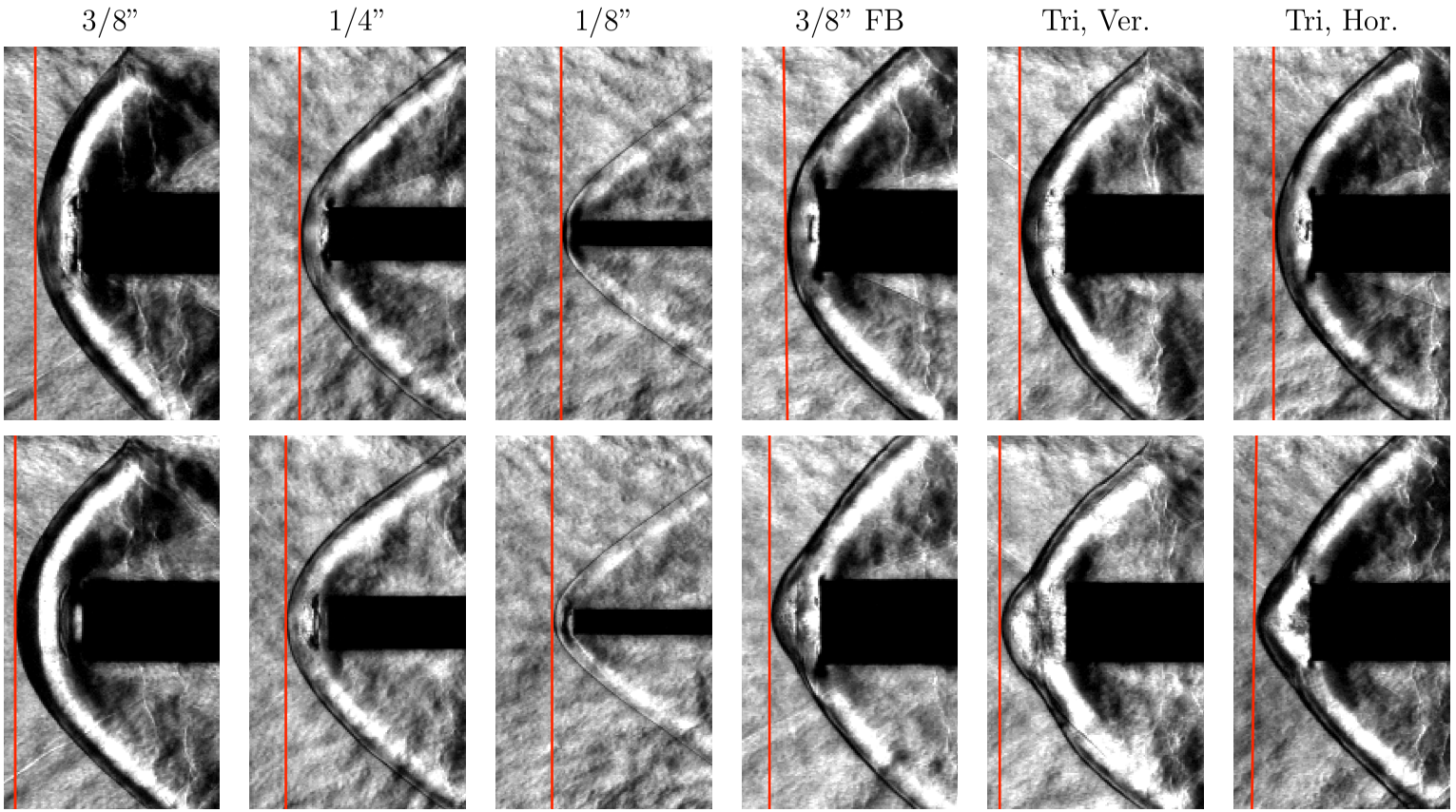

Figure 5.13: Snapshots of all unsteady cases showing the maximum shock displacement magnitude

Table 5.4: Fraction of the bow shock penetration time

Test case	Total number of frames	Number of frames of bow shock penetration	Fraction of bow shock penetration
1/8" Jet, 3/8" FB	833	143	17.2 %
Tri-nozzle, vertical	1024	83	8.1 %
Tri-nozzle, horizontal	1013	69	6.8 %

The magnitudes of the maximum bow shock displacements observed for unsteady cases are shown in Fig. 5.14. The maximum shock movement, Δx_{max} is normalized by the nozzle outer diameter, D_B. All distances are measured by counting pixels of each picture in Fig. 5.13. Regardless of the type of shock movement, with or without distortion of the shock smooth curvature, the magnitudes of the oscillation are very similar from one case to another. A small difference in shock penetration magnitude can be observed between two tri-nozzle orientations. Such difference could be the inherent nature introduced by the randomness of shock distortion. The maximum shock oscillation/distortion magnitude scales very well with the body diameter of each nozzle.

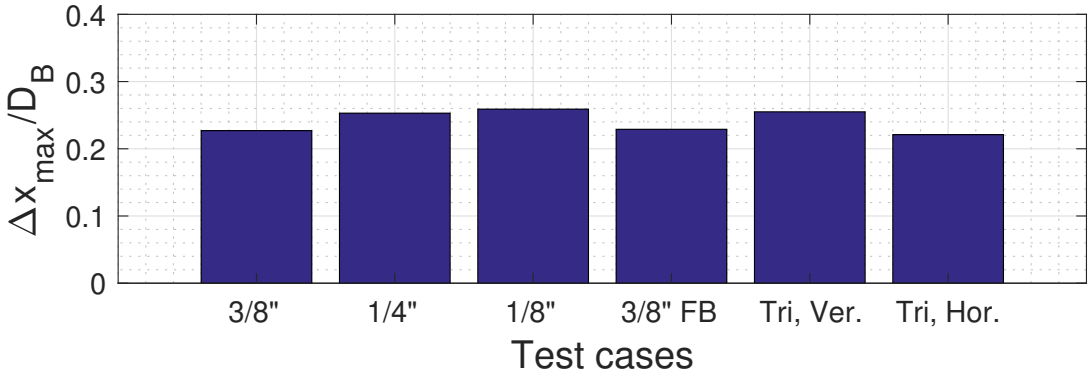

Figure 5.14: Normalized bow shock oscillation magnitude at P_0 ratio = 1

The similarity of the maximum magnitude of the bow shock displacement may suggest that both types of unsteady motions are the results of a similar mechanism. The visually more complex shock penetration is visually very different from the periodic shock oscillation observed for simple nozzles. This difference in dynamics may suggest that different mechanisms are the causes of these shock behaviors.

Chapter 6

CONCLUSION

This thesis experimentally investigated multi-nozzle supersonic retropropulsion flowfields at different jet pressures. The schlieren system at the University of Washington was enhanced to possess the capabilities of freezing flowfield structures with high consistency at high frequency and removing image doubling. A pulsed LED light source was developed and integrated with the high-speed motion capture system, so the motion blur was greatly reduced.

Based on a series of experiments, it was demonstrated that the tri-nozzle SRP flowfield is mostly similar to a single small nozzle with a forebody at the lowest jet pressure (P_0 ratio = 0.5). Tri-nozzle orientation was seen to cause an asymmetry in the bow shock radius that increased with jet pressure. Larger bow shock radius of curvature was observed in the direction parallel to the inline nozzles. At unity P_0 ratio, bow shock inflection points were observed in both directions of the tri-nozzle flowfield, indicating non-uniform bow shock motion.

Unsteady flowfields were experienced by all types of nozzles at unity stagnation pressure ratio, but with different features. The form of periodic shock oscillations was observed as unsteadiness on all simple nozzle flowfields. More erratic shock penetration and rippling were observed on tri-nozzle flowfields based on visual examinations, different from simple nozzles and similar to the 1/8" nozzle with 3/8" forebody. For all unsteady cases, normalized displacement magnitudes were very similar, within uncertainty, suggesting that both types of unsteadiness may share a common mechanism.

Between the tri-nozzle and 1/8" nozzle with 3/8" forebody, the similarity of unsteady modes and flowfields topology is likely due to the similarity of jet size relative to their

surrounding forebody. These similar features simplify the parameters to examine on the study of inline tri-nozzle, in which it suggests that at zero angle of attack, a single jet on a forebody is useful for closely approximate the dynamics and flowfield topology of an inline tri-jet. At a non-zero angle of attacks however, the tri-nozzle flowfield is likely to behave very differently compared to a single jet with a forebody.

Many aspects of inline tri-nozzle SRP flowfields remain to be examined. Oscillation and penetration magnitudes can be classified in greater detail. Frequencies of oscillation and penetration unsteady modes can be extracted and compared. Jet-to-jet interactions at highly under-expanded conditions where the barrel shock diameters are significantly larger than nozzle body diameters should also be tested. The dynamics of tri-nozzle SRP flowfields at an angle of attack should also be explored.

REFERENCES

[1] Fagin, M. H., *PAYLOAD MASS IMPROVEMENTS OF SUPERSONIC RETRO-PROPULSIVE FLIGHT FOR HUMAN CLASS MISSIONS TO MARS*, Master's thesis, Purdue University, West Lafayette, Indiana, December 2015.

[2] Korzun, A. M., Braun, R. D., and Cruz, J. R., "Survey of Supersonic Retropropulsion Technology for Mars Entry, Descent, and Landing," *JOURNAL OF SPACECRAFT AND ROCKETS*, Vol. 46 of *5*, AIAA, American Institute of Aeronautics and Astronautics, Inc., October 2009.

[3] Daso, E. O., Pritchett, V. E., Wang, T.-S., Ota, D. K., Blankson, I. M., and Auslender, A. H., "The Dynamics of Shock Dispersion and Interactions in Supersonic Freestreams with Counterflowing Jets," Tech. Rep. 1423, Reno, Nevada, January 2007.

[4] Tan, Y. M., *Influence of Pressure on Supersonic Retropropulsion Flow Field at Mach 2*, Master's thesis, University of Washington, Seattle, Washington, June 2018.

[5] Zilker, F., *Aerothermal Analysis of Re-usable First Stage during Rocket Retro-propulsion*, Master's thesis, Universitt Stuttgart, Institut fr Thermodynamik der Luft- und Raumfahrt (ITLR), Institute of Aerospace Thermodynamics (ITLR) Pfaffenwaldring 31, 1st floor 70569 Stuttgart, Germany, January 2018.

[6] Jarvine, P. O. and Adams, R. H., "TheAerodynamicCharacteristicsof Large Angled Cones with Retrorockets," Tech. Rep. CR NAS 7-576, NASA, Feb 1970.

[7] Ecker, T., Karl, S., Dumont, E., Stappert, S., and Krause, D., "A Numerical Study on the Thermal Loads During a Supersonic Rocket Retro-Propulsion Maneuver," 07 2017.

[8] Ecker, T., Zilker, F., Dumont, E., Karl, S., and Hannemann, K., "Aerothermal Analysis of Reusable Launcher Systems during Retro-Propulsion Reentry and Landing," May 2018.

[9] Korzun, A. M., Christopher E. Cordell, J., and Braun, R. D., "Comparison of Inviscid and Viscous Aerodynamic Predictions of Supersonic Retropropulsion Flowfields," Tech. Rep. 5048, Georgia Institute of Technology, Atlanta, GA, 30332, July 2010.

[10] Jarvinen, P. and Adams, R., "TheAerodynamicCharacteristicsof Large Angled Cones with Retrorockets," Tech. Rep. NASA-CR-124720, February 1970.

[11] Berry, S. A., Rhode, M. N., Edquist, K. T., and Player, C. J., "Supersonic Retropropulsion Experimental Results from the NASA Langley Unitary Plan Wind Tunnel," 5, AIAA, American Institute of Aeronautics and Astronautics, Inc., Honolulu, Hawaii, june.

[12] Wang, C.-M., *Transient Flow Analysis of a Supersinic Ludwieg-Tube Wind Tunnel*, Master's thesis, The University of Texas at Arlington, Arlington, Texas, May 1989.

[13] Settles, G. S., *Schlieren and Shadowgraph Techniques: Visualizing Phenomena in Transparent Media*, Springer-Verlag Berlin Heidelberg, Penn State University, Gas Dynamics Laboratory, 301 D Reber Building, University Park, PA 16802, 1st ed., 2001.

[14] Lincoln, D. A., *Development and Characterization of an LED-Based Light Source for High-Speed Schlieren Imaging*, Master's thesis, University of Calgary, Calgary, Alberta, January 2016.

[15] Finley, P. J., "The flow of a jet from a body opposing a supersonic free stream," *Journal of Fluid Mechanics*, Vol. 26, No. 2, 1966, pp. 337368.

[16] Berry, S. A. and Rhode, M. N., "Supersonic Retropropulsion Test 1853 in NASA LaRC Unitary Plan Wind Tunnel Test Section 2," Tech. rep., Langley Research Center, Hampton, Virginia, 4 2014.

[17] Wilson, S., Gustafson, G., D. Lincoln, K. M., and Johansen, C., "Performance evaluation of an overdriven LED for high-speed schlieren imaging," *Journal of Visualization*, Vol. 18, No. 1, February 2015, pp. 35–45.

[18] Ho, B., *Characterizing Unsteadiness in Supersonic Retropropulsion Flows*, Master's thesis, University of Washington, Seattle, Washington, June 2019.

[19] Korzun, A. M. and Braun, R. D., "Performance Characterization of Supersonic Retropropulsion for High-Mass Mars Entry Systems," Tech. Rep. 5, Georgia Institute of Technology, Georgia Institute of Technology, Atlanta, Georgia 30332, 2010.

[20] Willert, C., Stasicki, B., Klinner, J., and Moessner, S., "Pulsed operation of high-power light emitting diodes for imaging flow velocimetry," *Measurement Science and Technology*, Vol. 21, No. 7, June 2010.

Appendix A

PULSED LED CIRCUITS AND ASSOCIATED COMPONENTS

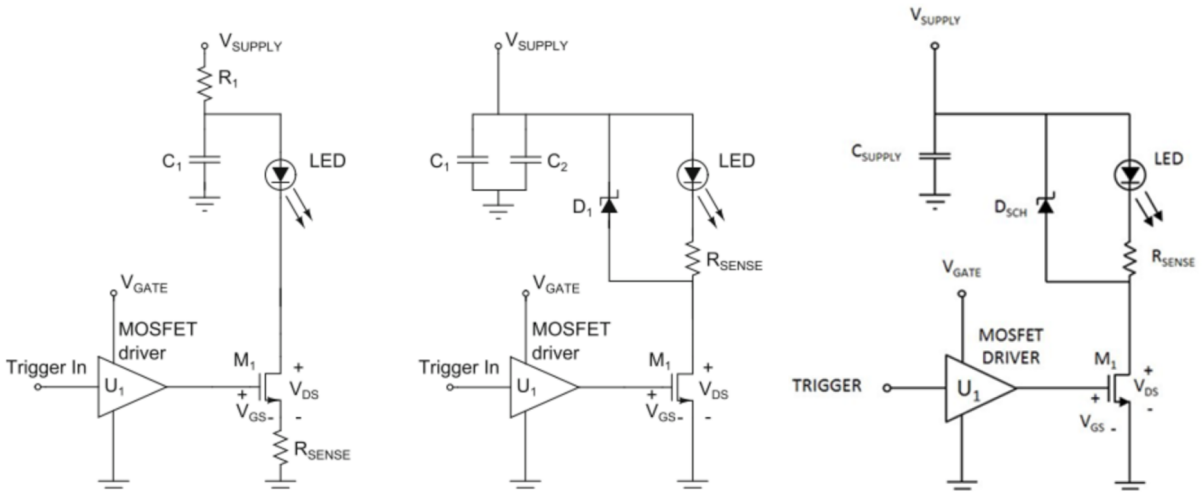

Figure A.1: Design iteration of the LED circuit by Willert et al. (2010b) (left) Wilson et al. (2014) (middle), and Lincoln (2016) (right)

Table A.1: Component list of pulsed LED circuits

Component	Willert et al. (2010)	Wilson et al. (2014)	Lincoln (2016)
C_1	1000 μF electrolytic	680 μF electrolytic	N/A
C_2	N/A	680 μF electrolytic	N/A
C_{SUPPLY}	N/A	N/A	B41560A8229M 22 mF capacitor
D_1	N/A	IDH20G65C6 Schottky Diode	IDH20G65C6 Schottky Diode
LED	CBT-120 Green LED	CBT-120 Green LED	CBT-120 Green LED
U_1	UCC37322P MOSFET driver	UCC37322P MOSFET driver	UCC37322P MOSFET driver
M_1	IRFB3206GPbF MOSFET	IRFB3206GPbF MOSFET	IRFB3206GPbF MOSFET
R_1	1 Ω	N/A	N/A
R_{SENSE}	0.02 Ω	0.005 Ω FCSL110R005FERCT	0.005 Ω FCSL110R005FERCT

Appendix B

BOW SHOCK STANDOFF DISTANCE NORMALIZED BY JET HYDRAULIC DIAMETER

Table B.1: Hydraulic diameter of each nozzle vs. their body diameter

	3/8" OD simple	1/4"OD simple	1/8" OD simple	1/8" jet + 3/8" FB	Tri-nozzle
Body Diameter, D_B	0.375"	0.250"	0.125"	0.375"	0.375"
Hydraulic Diameter, D_{hydro}	0.246"	0.168"	0.082"	0.082"	0.082"

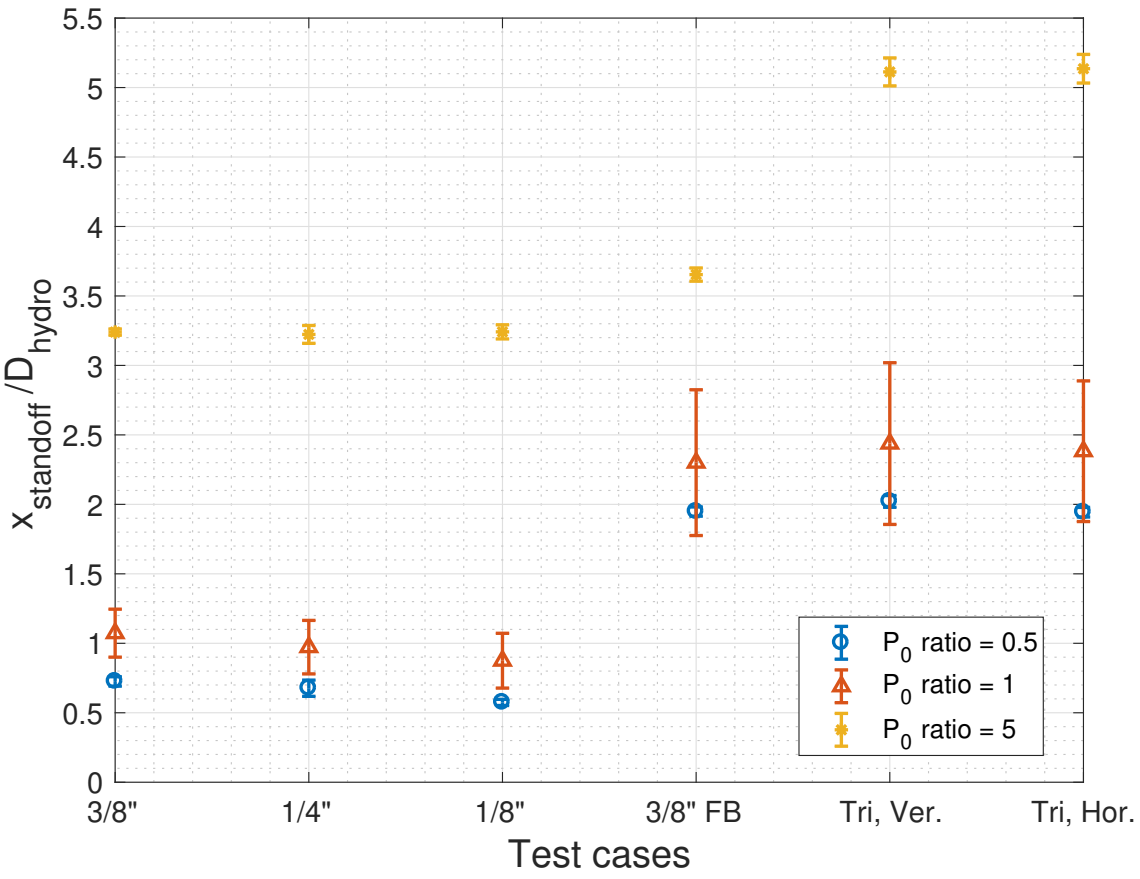

Figure B.1: Bow shock standoff distance normalized by jet hydraulic diameter